

An Ultradeep Multiband VLA Survey of the Faint Radio Sky (COSMOS-XS): Source Catalog and Number Counts

van der Vlugt, D.; Algera, H. S. B.; Hodge, J. A.; Novak, M.; Radcliffe, J. F.; Riechers, D. A.; Röttgering, H.; Smolčić, Vernesa; Walter, F.

Source / Izvornik: **The Astrophysical Journal, 2021, 907**

Journal article, Published version

Rad u časopisu, Objavljena verzija rada (izdavačev PDF)

<https://doi.org/10.3847/1538-4357/abcaa3>

Permanent link / Trajna poveznica: <https://urn.nsk.hr/urn:nbn:hr:217:011912>

Rights / Prava: [In copyright](#) / [Zaštićeno autorskim pravom.](#)

Download date / Datum preuzimanja: **2025-03-29**



Repository / Repozitorij:

[Repository of the Faculty of Science - University of Zagreb](#)





An Ultradeep Multiband VLA Survey of the Faint Radio Sky (COSMOS-XS): Source Catalog and Number Counts

D. van der Vlugt¹, H. S. B. Algera¹ , J. A. Hodge¹ , M. Novak² , J. F. Radcliffe^{3,4}, D. A. Riechers^{2,5} , H. Röttgering¹, V. Smolčić⁶, and F. Walter²

¹ Leiden Observatory, Leiden University, P.O. Box 9513, 2300 RA Leiden, The Netherlands; dvdvlugt@strw.leidenuniv.nl

² Max-Planck-Institut für Astronomie, Königstuhl 17, D-69117 Heidelberg, Germany

³ Jodrell Bank Centre for Astrophysics, The University of Manchester, SK11 9DL, UK

⁴ Department of Physics, University of Pretoria, Lynnwood Road, Hatfield, Pretoria 0083, South Africa

⁵ Department of Astronomy, Cornell University, Space Sciences Building, Ithaca, NY 14853, USA

⁶ Department of Physics, University of Zagreb, Bijenička cesta 32, 10002 Zagreb, Croatia

Received 2019 November 11; revised 2020 November 9; accepted 2020 November 13; published 2021 January 19

Abstract

We present ultradeep, matched-resolution Karl G. Jansky Very Large Array observations at 10 and 3 GHz in the COSMOS field: the COSMOS-XS survey. The final 10 and 3 GHz images cover ~ 16 and ~ 180 arcmin² and reach median rms values at the phase center of 0.41 and 0.53 μ Jy beam⁻¹, respectively. Both images have an angular resolution of $\sim 2''$. To account for the spectral shape and resolution variations across the broad bands, we image all data with a multiscale, multifrequency synthesis algorithm. We present source catalogs for the 10 and 3 GHz image with 91 and 1498 sources, respectively, above a peak brightness threshold of 5σ . We present source counts with completeness corrections included that are computed via Monte Carlo simulations. Our corrected counts at 3 GHz are consistent within the uncertainties with other results at 3 and 1.4 GHz but extend to fainter flux densities than previous direct detections. The 3 GHz number counts exceed the counts predicted by the semiempirical simulations developed in the framework of the SKA Simulated Skies project, consistent with previous $P(D)$ analyses. Our source counts suggest a steeper luminosity function evolution for faint star-forming sources. The semiempirical Tiered Radio Extragalactic Continuum Simulation predicts this steeper evolution and is in better agreement with our results at 10 and 3 GHz within the expected variations from cosmic variance. In summary, the multiband, matched-resolution COSMOS-XS survey in the COSMOS field provides a high-resolution view of the ultrafaint radio sky that can help guide next-generation radio facilities.

Unified Astronomy Thesaurus concepts: [Radio source counts \(1357\)](#); [Radio source catalogs \(1356\)](#); [Radio continuum emission \(1340\)](#)

1. Introduction

Over the last decade, a number of multiwavelength (UV to radio) studies have revealed that the star formation history of the universe (SFHU; i.e., the total star formation rate (SFR) per unit of comoving volume) went through several phases. The SFR apparently rose after the first galaxies formed (e.g., Bouwens et al. 2014, 2015) and reached its peak during the “epoch of galaxy assembly” at $1 \lesssim z \lesssim 3$. Subsequently, the SFR density declined rapidly to the present (e.g., Madau & Dickinson 2014 and references therein). It is well established that the majority of the star formation activity happens in galaxies that lie on the main sequence (MS), exhibiting an intrinsic scatter of ~ 0.3 dex, between SFR and stellar mass (e.g., Brinchmann et al. 2004; Elbaz et al. 2007; Noeske et al. 2007). Not only does the relation exist in the local universe (e.g., Brinchmann et al. 2004; Salim et al. 2007), but it is found to hold to $z \sim 4$ or even higher, albeit with a strong redshift evolution (e.g., Daddi et al. 2007; Pannella et al. 2009; Karim et al. 2011; Speagle et al. 2014; Schreiber et al. 2015; Salmon et al. 2015; Kurczynski et al. 2016; Tomczak et al. 2016). An accurate measurement of the SFR and its relation to stellar mass at all epochs is key for a better understanding of galaxy evolution.

Several tracers across the electromagnetic spectrum can be used to measure this SFR, each with their own unique strengths and weaknesses. For example, ultraviolet (UV) light originates mainly from massive stars and thus directly traces young stellar

populations. However, UV-based observations need uncertain and significant model-dependent dust corrections to account for dust obscuration (e.g., Carilli et al. 2008; Siana et al. 2008, 2009; Chary & Pope 2010; Magdis et al. 2010; Bouwens et al. 2012). Infrared (IR) observations trace the absorbed UV emission that is thermally reprocessed by dust surrounding newly formed stars. However, the resolution of IR observations is often insufficient to provide reliable multiwavelength identifications. In addition, the presence of polycyclic aromatic hydrocarbon (PAH) emission features redshifted ($z > 0.8$) into the 24 μ m band, commonly used as an estimator for the total IR emission, makes the required k -correction uncertain.

Long-wavelength radio emission is another potential tracer of recent star formation (Condon 1992). Radio emission in galaxies below rest-frame frequencies $\lesssim 30$ GHz is dominated by synchrotron radiation arising from cosmic-ray electrons gyrating in the galaxy magnetic fields (e.g., Sadler et al. 1989; Condon 1992; Clemens et al. 2008; Tabatabaei et al. 2017). These charged cosmic-ray particles are accelerated in shocks launched by supernovae of stars with $M > 8 M_{\odot}$ in star-forming galaxies (SFGs). These massive stars have lifetimes of $\lesssim 3 \times 10^8$ yr, so their supernova rates are proportional to the recent SFR. This is supported by the tight correlation observed in SFGs between IR emission, originating from dust that has been heated by young and massive stars, and radio emission (the IR–radio correlation; e.g., de Jong et al. 1985; Helou et al. 1985; Yun et al. 2001; Bell 2003; Dumas et al. 2011).

Deep radio observations in the synchrotron regime can thus be used to constrain SFRs. Radio observations can also provide high spatial resolution to allow for reliable counterpart matching. Distant galaxies in the gigahertz radio regime often have spectral energy distributions (SEDs) that can be parameterized by a featureless power law, leading to a simple and robust k -correction. Radio observations in the synchrotron regime thus offer a unique opportunity to study the SFHU (e.g., Condon et al. 2002; Seymour et al. 2008; Smolčić et al. 2009a; Jarvis et al. 2015; Calistro Rivera et al. 2017; Novak et al. 2017) at a wavelength that is free from selection biases due to dust obscuration.

However, there are two challenges in using radio emission in the synchrotron regime as a tracer of star formation. The first is the “contamination” by active galactic nuclei (AGNs). It is hard to disentangle AGNs and SFGs in the radio regime, as an accreting supermassive black hole (SMBH) in an AGN can also accelerate the electrons that produce synchrotron emission. To attempt to correct for this, several methods have been developed for identifying different types of AGNs and separating them from SFGs (e.g., Hickox et al. 2009; Mendez et al. 2013; Delvecchio et al. 2017; Smolčić et al. 2017a; Algera et al. 2020) using mid- and far-IR (FIR) data, X-ray information, and multiband optical/IR photometry. Synchrotron emission can thus not only be used to study star formation but also to study the black hole accretion activity in the universe (e.g., Jarvis & Rawlings 2000; Smolčić et al. 2009b; Rigby et al. 2011; McAlpine et al. 2013; Best et al. 2014; Delvecchio et al. 2014, 2017; Sabater et al. 2019).

The second challenge is the depth achievable in radio surveys. With the improving capabilities of modern interferometers, along with sophisticated calibration techniques, surveys of the faint microjansky radio-emitting objects are able to constrain the faint populations (e.g., Rujopakarn et al. 2016; Murphy et al. 2017; Smolčić et al. 2017b; Bondi et al. 2018; Owen 2018; Mauch et al. 2020). At high flux densities, the source counts are well constrained and found to be dominated by AGNs that follow a smooth power-law distribution down to $S_{1.4\text{ GHz}} \sim 1\text{ mJy}$ (e.g., Condon & Mitchell 1984; Windhorst et al. 1990). Below 1 mJy, the Euclidean-normalized source counts flatten (e.g., Richards 2000; Huynh et al. 2005; Biggs & Ivison 2006; Bondi et al. 2008; Owen & Morrison 2008; Padovani et al. 2015). It is now widely accepted that this observed flattening is due to the emergence of SFGs and radio-quiet (RQ) AGNs, which begin to contribute significantly (e.g., Rowan-Robinson et al. 1993; Seymour et al. 2004; Padovani et al. 2009). New deep radio observations and $P(D)$ analyses of confusion-limited surveys show evidence of a further steepening of the number counts below $S_{1.4\text{ GHz}} \sim 50\text{ }\mu\text{Jy}$ (e.g., Condon et al. 2012; Vernstrom et al. 2014, 2016; Smolčić et al. 2017b; Prandoni et al. 2018; Mauch et al. 2020). The composition of this ultrafaint radio population is still uncertain, but it is expected from simulations and observations that the fraction of SFGs will become significant ($>60\%$) below $S_{1.4\text{ GHz}} \sim 100\text{ }\mu\text{Jy}$ (Smolčić et al. 2017a). Constraints on the ultrafaint radio populations at high resolution are useful for predictions for future radio surveys with new and upcoming facilities, such as the ASKAP, MeerKAT, ngVLA, and SKA, where source confusion noise may be an issue.

Survey depth is also a challenge for radio surveys at observing frequencies $\geq 10\text{ GHz}$. Such surveys measure flux

densities closer to the rest-frame frequencies $\nu \geq 30\text{ GHz}$, where the total radio emission is dominated by free-free radiation (e.g. Condon 1992; Murphy et al. 2011; Klein et al. 2018) that constitutes the faintest part of the radio SED. Although more difficult to detect, free-free emission provides independent information on the star formation process. Free-free emission directly originates from the H II regions where massive stars form and thus provides a firsthand view of star formation. In addition, unlike UV emission, dust obscuration plays only a minor role; therefore, free-free emission is potentially the most accurate tracer of star formation (e.g., Mezger & Henderson 1967; Turner & Ho 1983, 1985; Klein & Graeve 1986; Kobulnicky & Johnson 1999; Murphy et al. 2012, 2015; Nikolic & Bolton 2012).

A limitation on high-frequency observations is the smaller primary beam area, as this area decreases with frequency ($\Omega_{\text{pb}} \propto \nu^{-2}$). This limits the area that is covered at a certain depth. Low frequencies have therefore been favored, and radio continuum surveys probing free-free emission are still sparse in the literature.

The majority of extragalactic radio surveys are conducted at 1.4 and 3 GHz, where the radio emission of galaxies is intrinsically brighter than at higher frequencies, and large areas can be imaged with a single pointing. In the last decade, several studies have been conducted to trace the synchrotron emission from galaxies (e.g., Schinnerer et al. 2007, 2010; Morrison et al. 2010; Smolčić et al. 2017b; Prandoni et al. 2018). The COSMOS field has been observed with the Very Large Array (VLA) at 1.4 GHz ($\sigma \sim 10\text{--}15\text{ }\mu\text{Jy beam}^{-1}$; Schinnerer et al. 2010) and more recently at 3 GHz with substantially better sensitivity ($\sigma \sim 2.3\text{ }\mu\text{Jy beam}^{-1}$), yielding about four times more radio sources compared to the 1.4 GHz data (Smolčić et al. 2017b); see Figure 1. Although these observations provide valuable data over the entire 2 deg^2 COSMOS field, enabling some of the most comprehensive studies to date of the SFG and radio AGN population, they are equivalent to $\sim 2\text{ hr}$ pointing $^{-1}$. The resulting sensitivity only allows for the detection of typical SFGs out to $z \sim 1.5$ (Novak et al. 2017), the epoch where the various star formation tracers begin to diverge (e.g., Ilbert et al. 2013). In order to observe MS galaxies over the full epoch of galaxy assembly ($z \sim 1\text{--}3$), a submicrojansky survey is essential.

The significantly increased bandwidths of the upgraded NSF Karl G. Jansky VLA now allow for observations of the radio sky down to several hundred nJy beam^{-1} sensitivities. We have taken advantage of these recent upgrades to the VLA to do an ultradeep matched-resolution survey in both the X and S bands (10 and 3 GHz). This COSMOS-XS survey is one of the deepest radio surveys to date, reaching submicrojansky sensitivities, and is \sim five times deeper than the previous 3 GHz observations conducted in the COSMOS field (Smolčić et al. 2017b). When combined with the rich COSMOS multiwavelength data, this survey thus yields a unique data set to test the composition of the faintest radio source populations that can currently be probed.

The combined S- and X-band observations will enable us to study the properties and importance of AGNs and SFGs in a dust-unbiased way and make predictions for the populations to be detected by future surveys. This paper (hereafter Paper I) describes the 10 and 3 GHz observations and examines their implications for the ultrafaint source counts. In a companion

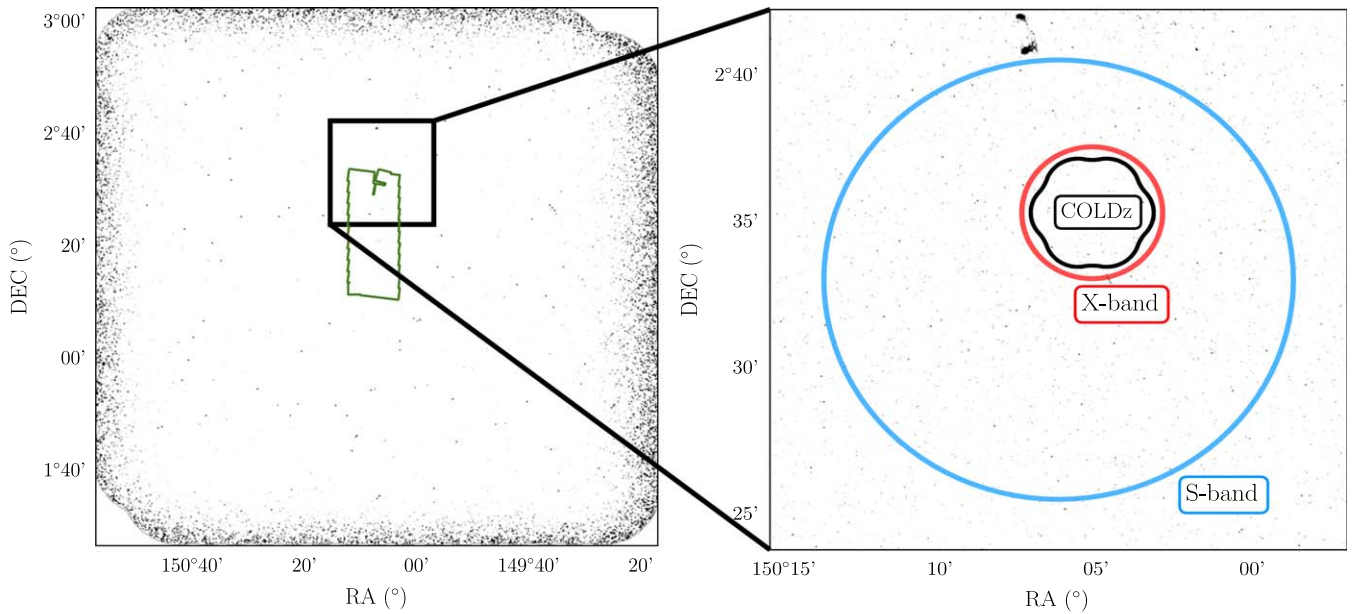


Figure 1. Full 3 GHz mosaic as imaged by Smolčić et al. (2017b) of the 2 deg² COSMOS field. The green polygon indicates the footprint of the CANDELS WFC3 imaging (Nayyeri et al. 2017). The inset of 340 arcmin² shows the position of the X- and S-band primary beam. Additionally, the seven-pointing mosaic at 34 GHz, part of the COLDz project (Pavesi et al. 2018), is shown with the black contour.

Table 1
10 and 3 GHz Pointing Centers and Total Observing Time

Band	Central Frequency (GHz)	Configuration	Center (J2000)		Total Integration Time (hr)	Primary Beam FWHP (arcmin)	Central rms (μ Jy)
			R.A.	Decl.			
S	3	B	10 ^h 00 ^m 25 ^s	+02°33′00″	100	15	0.53
X	10	C	10 ^h 00 ^m 20.7	+02°35′17″	90	4.5	0.41

paper (Algera et al. 2020; hereafter Paper II), we match the obtained catalogs with the multiwavelength data available in the COSMOS field to distinguish between AGNs and SFGs. The obtained populations are then used to constrain the composition of the ultrafaint source counts.

This paper is organized as follows. In Section 2, we describe the VLA 10 and 3 GHz observations, calibration, imaging, and catalog extraction. In Section 3, we present the final images and describe the source detection method and the compilation of the source catalog. This section also includes an analysis of the quality of the catalog. In Section 4, we discuss the derivation of the completeness-corrected radio source counts. Finally, Section 5 summarizes and concludes this work. Throughout this paper, the spectral index, α , is defined as $S_\nu \propto \nu^\alpha$, where S is the source flux density, and ν is the observing frequency. We assume a spectral index of -0.7 unless otherwise stated.

2. Observations and Data Reduction

2.1. Observations

The COSMOS-XS survey (see Table 1) consists of the combination of a single deep S-band pointing centered on R.A. = 10:00:25, decl. = +02°33′00″ (see Figure 1) in the B configuration and an additional single X-band pointing observed in the C array centered on the COSMOS/AzTEC-3 protocluster at $z \sim 5.3$, coordinates R.A. = 10:00:20.7, decl. = 02°35′17″ (see Figure 1). The chosen configurations provide a resolution of $\sim 2''$ in the X and S bands, which is large enough to avoid resolving out faint sources. The X-band

survey overlaps with the COLDz survey (Pavesi et al. 2018; Riechers et al. 2019), one of the deepest 34 GHz continuum surveys, covering ~ 10 arcmin², to date. The S-band pointing is chosen to be slightly offset from the X-band pointing to overlap more with the CANDELS-COSMOS field (Nayyeri et al. 2017). The X and S bands were observed for 90 and 100 hr, respectively. These data were taken between 2014 December 4 and 2016 February 27 with the individual observations constituting either 2 or 5 hr observing blocks. For the X-band observations, J1024–0052 was used as the phase calibrator, while for the S-band observations, J0925+0019 was used. For both bands, 3C 286 served as both the flux and bandpass calibrator. The X band covers a bandwidth of 4096 MHz centered at 10 GHz and is separated into 32 spectral windows (SPWs) 128 MHz wide. All four polarization products were recorded, and a 2 s signal-averaging time was used. The S band covers a bandwidth of 2048 MHz centered at 3 GHz and is separated into 16 SPWs 128 MHz wide. Again, all four polarization products were recorded, and a 5 s signal-averaging time was used.

2.2. Calibration

The calibration of the X- and S-band visibilities was performed using CASA⁷ version 5.0.0. Extensive use was made of the NRAO VLA reduction pipeline.⁸ Radio frequency

⁷ <http://casa.nrao.edu/>

⁸ <https://science.nrao.edu/facilities/vla/data-processing/pipeline>

interference (RFI) constitutes the major uncertainty in our data calibration. We experimented with different methods and tools (`rflag`, `AOflogger`; Offringa 2010) to remove the RFI. However, the unmodified pipeline resulted in the best image.

Before running the pipeline, Hanning smoothing was applied to lessen Gibbs ringing from strong spectral features such as strong, narrow RFI. The pipeline runs several flagging rounds to flag bad or unnecessary data, such as the initial few integration points of a scan where not all antennas may be on source. To flag RFI, the pipeline performed several rounds of flagging using the `rflag` algorithm. The pipeline used the `gencal` and `gaincal` tasks to derive the necessary calibration solutions; `setjy` was used to set the flux scale of the observations (Perley & Butler 2013), and the flux density calibrator was 3C 286. During the calibration, no time or bandwidth averaging was performed so as to minimize time and bandwidth-smearing effects (see Section 2.3).

In the *X* band, two SPWs, SPW 32 and SPW 33, were heavily flagged (>85%) because of RFI. For the *S* band, only SPW 4 was found to be heavily corrupted by RFI and was flagged almost entirely by the pipeline. After the pipeline was run on the 10 and 3 GHz data, the target field was split off using the task `split`, and, respectively, 24.9% and 25.8% of the split off data were flagged.

2.3. Bandwidth and Time Smearing

An antenna receiver has a finite bandwidth, which causes bandwidth smearing. This effect radially smears peak brightness while the integrated flux densities are conserved. Bandwidth smearing is a function of distance from the pointing center. The theoretical prediction from Condon et al. (1998) for the reduction of peak response is given by $I/I_0 = 1/\sqrt{1 + 0.46\beta^2}$, where $\beta = (\Delta\nu/\nu_0) \times (\theta_0/\theta_{\text{HPBW}})$. If we calculate the reduction at 20% of the peak primary beam sensitivity using the VLA channel width $\Delta\nu = 2$ MHz, central frequency $\nu_0 = 3$ GHz, and a beam size of $\theta_{\text{HPBW}} = 2''$, we find an offset of $\sim 1\%$. When we compare the peak brightness over the total flux density for pointlike sources ($0.9 \leq S_{\text{peak}}/S_{\text{int}}$) with a signal-to-noise ratio (S/N) > 6 as a function of distance from the pointing center, we find that an offset of $\sim 4\%$ is present. This is, however, not distance-dependent and thus unlikely to be related to bandwidth smearing.

For the 10 GHz observations, we calculate a reduction of $\sim 0.01\%$ at 20% of the peak primary beam sensitivity using the VLA channel width $\Delta\nu = 2$ MHz, central frequency $\nu_0 = 10$ GHz, and a beam size of $\theta_{\text{HPBW}} = 2''$. The $S_{\text{peak}}/S_{\text{int}}$ distribution of pointlike sources ($0.9 \leq S_{\text{peak}}/S_{\text{int}}$) with S/N > 6 with distance also shows no distance-dependent offset. Therefore, we do not apply any corrections at 10 and 3 GHz for the bandwidth-smearing effect.

The individual observations were concatenated after the calibration steps using the CASA task `concat`. These data were subsequently averaged in time using `split` with an averaging time of 21 s for the *X* band and 6 s for the *S* band. Averaging visibility data in the time domain causes a similar distortion to bandwidth smearing, but in the opposite direction (i.e., tangentially). The averaging time used should lead to an amplitude loss of at most 1% for a point source located at the first null of the primary beam due to loss of coherence.⁹

⁹ <https://science.nrao.edu/facilities/vla/docs/manuals/oss2013B/performance/fov/t-av-loss>

Table 2

Overview of the Wide-field Imaging Parameters for the 10 and 3 GHz Image

Band	Robust	Pixel Size (arcsec)	<i>w</i> Planes	Restoring Beam (arcsec)
<i>S</i>	0.5	0.4	400	2.14×1.81
<i>X</i>	0.5	0.42	128	2.33×2.01

2.4. Imaging

Imaging of the concatenated data sets was performed both with the CASA task `clean` and the stand-alone imaging algorithm `WSclean` (Offringa et al. 2014). For our purposes, the main difference between the two algorithms is the method of taking into account the interferometric *w* term during deconvolution. We opted for `WSclean` to create the final images based on its faster processing compared to CASA's `clean`. However, the differences between the CASA `clean` and `WSclean` images are minimal (see also Offringa et al. 2014); hence, the choice of algorithm has no effect on the end product.

`WSclean` produces images by jointly gridding and deconvolving the measurement set, which is called joined-channel deconvolution (Offringa & Smirnov 2017). The spectral behavior of sources can be captured during deconvolution by setting the parameters `-channels-out` and `-join-channels`. The data are then imaged in separate channels across the band. During deconvolution, `WSclean` finds peaks in the full-band image and deconvolves these in each channel independently.

For the 10 GHz image, we weight our image via Briggs weighting with a robust parameter of 0.5 (Briggs 1995) and apply *w* stacking using the minimum recommended number of 128 layers (`-nwlayers`). We use the joined-channel deconvolution technique, specified by setting `-channels-out` to 32 (i.e., one per SPW) and specifying the parameter `-join-channels`. A power law is fit to account for in-band spectral variations (similar to the multiterm, multifrequency synthesis algorithm used in CASA's `tclean` with `nterms = 2`; Rau & Cornwell 2011). In addition, we utilize automasking of sources after first cleaning down to 3σ , whereupon masked sources are further cleaned down to 0.5σ (parameters `-auto-mask` and `-auto-threshold`, respectively). The combination of these settings for `-auto-mask` and `-auto-threshold` is a good general setting for `WSclean`, which leaves almost no residuals behind. The resulting image reaches an rms sensitivity of $\sigma = 0.41 \mu\text{Jy beam}^{-1}$ (Table 2).

For the 3 GHz image, we take a similar approach to that described above but with a few changes in the imaging parameters. The number of layers for *w* stacking is increased to 400. We find that *w*-term artifacts persist for imaging with 128 layers, and increasing the number to 400 solves these issues. We also do not fit the spectral variations with a power law because of the large noise fluctuations at the beam edge caused by a bright source (see Figure 4). The `-channels-out` parameter is set to 16 (i.e., one per SPW). The resulting image reaches an rms sensitivity of $\sigma = 0.53 \mu\text{Jy beam}^{-1}$ (Table 2).

Because primary beam correction via projection-based gridding is not yet operational, we take the primary beam model from the CASA `widebandpbcor` task,¹⁰ which takes the frequency dependence of the beam into account.

¹⁰ This task was run by means of CASA version 5.3, which has an updated beam shape model.

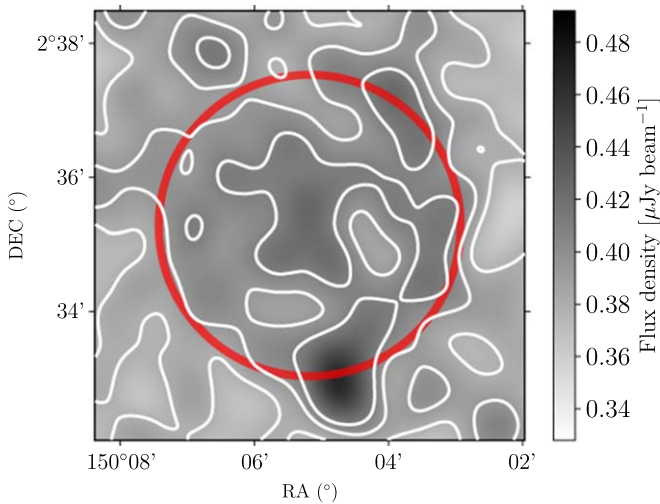


Figure 2. The rms map of the 10 GHz observation before primary beam correction. The image size is 41 arcmin². The rms map is created with PyBDSF. The red circle indicates the HPBW of the primary beam at 10 GHz, which corresponds to 4.5 . The gray scale shows the rms noise from 0.8σ to 1.2σ , where $\sigma = 0.41 \mu\text{Jy beam}^{-1}$. The contours are plotted at $[0.38, 0.39, 0.41] \mu\text{Jy beam}^{-1}$.

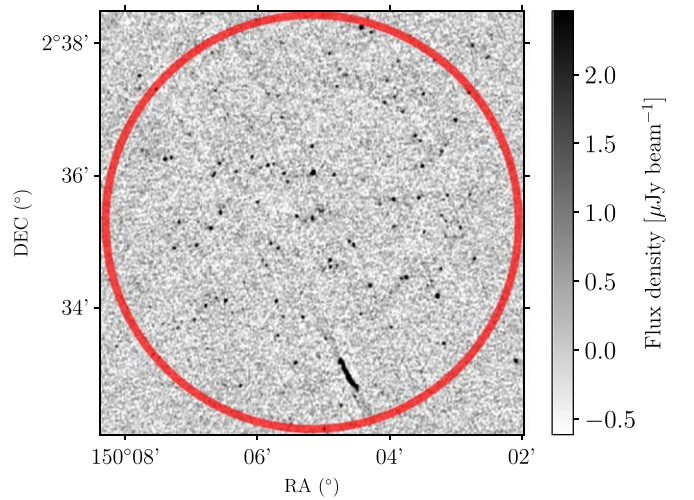


Figure 3. Final calibrated 10 GHz image before primary beam correction. The size is the same as in Figure 2. The red circle indicates the point where the primary beam sensitivity is 20% of its peak. The gray scale shows the flux density from -1.5σ to 6σ , where $\sigma = 0.41 \mu\text{Jy beam}^{-1}$ is the median rms within the primary beam FWHP. The corresponding brightness temperature rms value is $\sigma = 1.25 \text{ mK}$. The image is matched in resolution and depth for a spectral index of -0.7 with the 3 GHz image.

2.5. Confusion

Finally, we note that the source confusion is negligible in the deep 3 GHz VLA observation (only the *S*-band image is considered, as it has the highest source density). The beam size is $2''.14 \times 1''.81$, which results in $3.16 \times 10^6 \text{ beams deg}^{-2}$. At the faintest flux density bin of our number count measurements for the *S* band (see Section 4.1.6), we find $\sim 1 \times 10^4$ sources deg^{-2} . This translates to one source per ~ 316 beams and implies that confusion is not an issue. Following Condon et al. (2012), source confusion becomes important at one source per 25 beams. This confusion limit depends on the slope of the scale-free power-law approximation for the number counts,

$$n(S) = kS^{-\gamma}, \quad (1)$$

where K is the count normalization and $1 < \gamma < 3$ is the differential count slope (Condon et al. 2012). For the calculation of the confusion limit, we assumed a slope of $\gamma = 2.0$. We expect source confusion to contribute approximately $0.01 \mu\text{Jy beam}^{-1}$ to the noise following Equation (27) from Condon et al. (2012).

3. Final Image and Cataloging

The final 10 and 3 GHz images are shown in Figures 3 and 5, respectively. The central rms noise level is relatively smooth for both images (see also Figures 2 and 4). The 3 GHz image shows a small number of artifacts (see, e.g., the northern part of the image shown in Figure 5). The artifacts are localized around bright sources and have little impact on the majority of the map, as can be seen from Figure 4.

3.1. Source Detection and Characterization

We compiled a source catalog using PyBDSF¹¹ (Mohan & Rafferty 2015) to detect and characterize sources. We ran PyBDSF on the final image using the pre-primary-beam-corrected image as the detection image.

PyBDSF identifies peaks of emission above a given threshold (`thresh_pix`) that are surrounded by contiguous pixels with emission greater than a minimum (`thresh_isl`). It fits the identified island with one or more Gaussians, which are subsequently grouped into sources. This happens if all of the pixels on the line joining their centers have a value greater than `thresh_isl` and the length of this line is less than half the sum of their FWHMs. The total flux density of the sources is estimated by adding those from the individual Gaussians, while the central position and source size are determined via moment analysis.

The spatial variation of the image noise was estimated by sliding a box across the image in overlapping steps, calculating the rms of the pixels within the box and interpolating the values measured from each step. The resulting rms map provides PyBDSF with an estimate of the spatial variation of the image noise for detection thresholding purposes. The rms maps for the 10 (see Figure 2) and 3 (see Figure 4) GHz images are determined with a sliding box of `rms_box` = (120, 60) and (400, 100) pixels (i.e., a box size of 400 pixels every 100 pixels), respectively.

For source extraction, we used `thresh_pix` = 5.0σ and `thresh_isl` = 3.0σ (i.e., the limit at which flux density is included in the source for fitting). Figures 2 and 4 illustrate the variation in rms noise determined across the image and show the increase in local rms as a result of calibration artifacts near bright sources. We used the `group_tol` parameter with a default value of 1.0. A higher value for this parameter allows larger sources to be fitted. Sources are classified as “S” for single sources and “M” for multiple Gaussian sources. The parameters of the Gaussian fitted to the source are reported by PyBDSF.

For the 10 GHz (3 GHz) images, the total number of sources detected by PyBDSF within 20% of the peak primary beam sensitivity is 93 (1498), of which 90 (1392) are single-component sources, or sources fitted by a single Gaussian.

¹¹ <http://www.astron.nl/citt/pybdsf/>

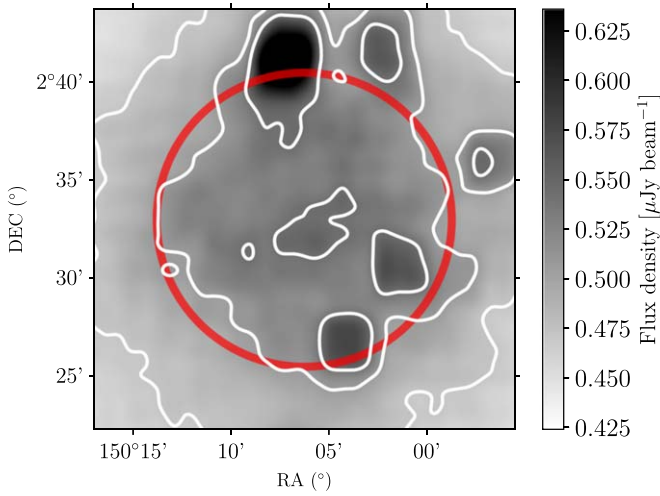


Figure 4. The rms map of the 3 GHz observation before primary beam correction. The image size is 460 arcmin². The rms map is created with PyBDSF. The red circle indicates the HPBW of the primary beam at 3 GHz, which corresponds to 15'. The gray scale shows the rms noise from 0.8σ to 1.2σ , where $\sigma = 0.53 \mu\text{Jy beam}^{-1}$. The contours are plotted at [0.47, 0.51, 0.54] $\mu\text{Jy beam}^{-1}$.

3.2. Resolved Sources

In order to determine whether our identified source components are resolved, we make use of the ratio between integrated flux density (S_{int}) and peak brightness (S_{peak}), which is a direct measure of the extension of a radio source. For an unresolved source, the peak brightness equals the total flux density. Noise influences the measurements of S_{int} and S_{peak} ; therefore, the $S_{\text{int}}/S_{\text{peak}}$ distribution gets broadened toward the low-S/N end. The effect of noise on the $S_{\text{int}}/S_{\text{peak}}$ ratio can be determined by performing Monte Carlo simulations in which simulated sources are added to the pre-primary-beam-corrected image and then retrieved the same way as the observed data. We simulate 100 mock sources and insert these into the real image. This is repeated 200 times, simulating 20,000 sources in total. The method described below is used to derive the upper envelope of the $S_{\text{int}}/S_{\text{peak}}$ distribution for both the 10 and 3 GHz image.

Sources are injected as Gaussians with their FWHM equal to the beam size, and they are thus unresolved by construction. We only insert point sources to quantify how the noise “resolves” unresolved sources. The peak brightnesses of the sources are drawn from the real source distribution to generate a realistic mock catalog. We fit a power law of the form $n = a \times S^{-\gamma} + b$ (see Equation (1)) to the binned measured peak brightness distribution and draw fluxes between 3σ and 60σ randomly from this distribution. The mock sources are assigned a position that is at least 20 pixels ($\sim 8''$) away from both real sources and other mock sources. The position of the mock source also has to lie within the 20% power point of the primary beam. The position is randomly chosen until both restrictions are satisfied.

After all mock sources are inserted, we run PyBDSF with the exact parameters as performed for the real sources. Since the extraction is carried out on a map containing both real and mock emission, the real sources are always recovered and have to be filtered out in order to keep only simulated sources in the extracted catalog.

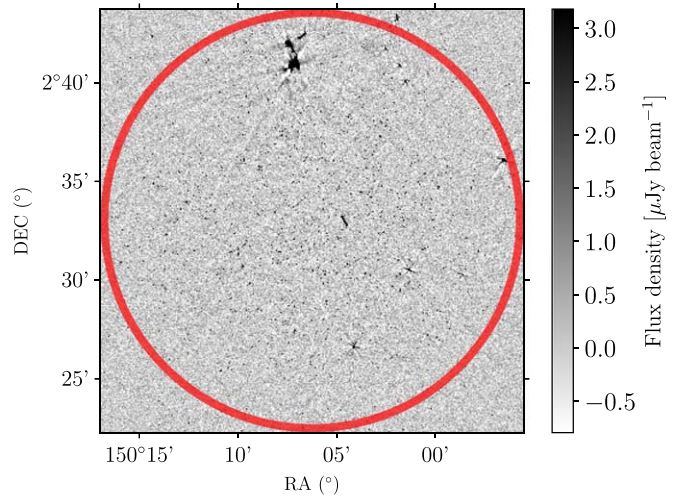


Figure 5. Final calibrated 3 GHz image before primary beam correction. The size is the same as in Figure 4. The red circle indicates the point where the primary beam sensitivity is 20% of its peak. The gray scale shows the flux density from -1.5σ to 6σ , where $\sigma = 0.53 \mu\text{Jy beam}^{-1}$ is the median rms within the primary beam FWHP. The corresponding brightness temperature rms value is $\sigma = 18.0 \text{ mK}$.

The recovered $S_{\text{int}}/S_{\text{peak}}$ distribution as a function of S/N is shown in Figure 6. To determine the 95% envelope in Figure 6, a curve (red line) is fitted to the 95th percentile of logarithmic bins across the S/N, where $N = \sigma_{\text{local}}$ as measured by PyBDSF. The shape of the envelope was chosen following Bondi et al. (2008). The fit for the 10 GHz image simulations is given by $S_{\text{int}}/S_{\text{peak}} = 1.14 + 11.6 \times (\text{S/N})^{-1.64}$. The fit for the 3 GHz image simulations is given by $S_{\text{int}}/S_{\text{peak}} = 1.07 + 14.0 \times (\text{S/N})^{-1.69}$.

We consider sources from our catalog that lie above this envelope to be resolved. For the 10 GHz image, there are 12 (13%) resolved sources, and for the 3 GHz image, there are 475 (32%) resolved sources. For sources that lie under the envelope, the integrated flux density was set equal to the peak brightness. The resolved sources are flagged as resolved in the final catalog presented in Section 3.8. Note that not all of the PyBDSF sources with multiple Gaussian components are resolved by this criterion, as each component is considered separately. Conversely, not all single-component sources are unresolved.

3.3. Flux Boosting

The noise fluctuations in the image may influence the flux measurements of the extracted sources. Since the counts of faint sources increase with decreasing flux density, there should be a sea of faint sources below the noise level that may influence the source extraction. There is, therefore, a probability that intrinsically faint sources are detected at higher flux because of noise fluctuations. This effect, called flux boosting, is extremely important at low S/N, where flux measurement can be overestimated.

The degree of flux boosting (the probability that faint sources are detected at higher flux density because of noise fluctuations) can be estimated by examining the output-to-input flux density of the simulations described in the above section. Figure 7 shows the distribution of the recovered flux density minus the inserted flux density normalized by the inserted flux

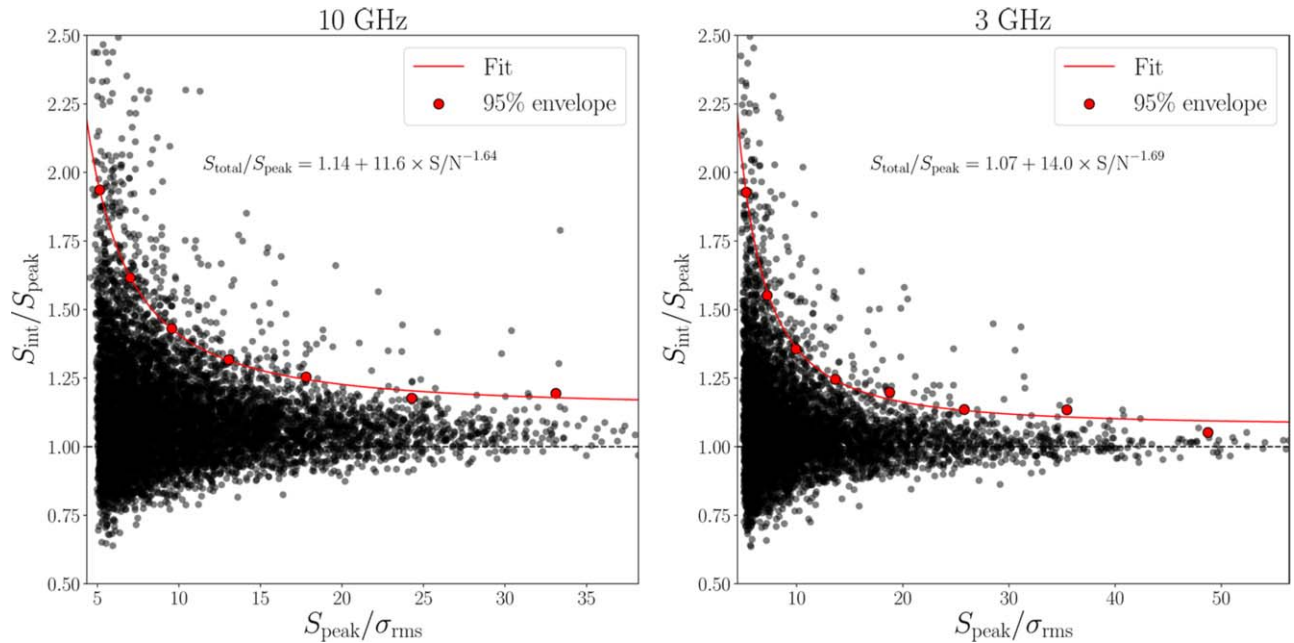


Figure 6. Simulated ratio of integrated flux density to peak brightness as a function of S/N for unresolved sources from the 200 Monte Carlo simulations for the 10 (left) and 3 (right) GHz images. For logarithmic bins in S/N, the red points show the threshold below which 95% of the sources lie in that bin. The red line shows the fit to this upper envelope. Applying these thresholds to the real data, we find that, respectively, 13% and 32% of the sources are resolved.

density as a function of recovered flux density, where we calculated the mean and standard deviation in logarithmic bins.

The effect of flux boosting is, as expected, greatest at the flux limit of our survey. For the 10 GHz (3 GHz) image, sources with $S/N \simeq 5$ are boosted by 11% (15%), on average. The boosting effect quickly decreases with S/N; we find that sources with $S/N \simeq 10$ are boosted by less than 5%, on average. Therefore, we do not correct for flux boosting.

3.4. Flux Density Uncertainties at 3 GHz

In order to determine any systematic offsets, we have compared our flux densities to those of the VLA-COSMOS 3 GHz Large Project. For the comparison, we selected only sources that could be detected at high S/N in the VLA-COSMOS 3 GHz Large Project catalog, which has a flux density limit of $S/\sigma > 5 = 11.5 \mu\text{Jy}$. We also consider only unresolved sources in the VLA-COSMOS 3 GHz Large Project catalog to rule out resolution effects. This yielded a sample of 250 objects. For this subsample of sources, we determined the ratio of peak brightness between the COSMOS-XS survey and the VLA-COSMOS 3 GHz Large Project, $f_S = S_{\text{COSMOS-XS}}/S_{\text{Smolcic+2017}}$. The result of this comparison is shown in Figure 8. We measured a median ratio of 0.98 with a standard deviation of 0.18. The plot shows that the flux scale is in good agreement with the VLA-COSMOS 3 GHz Large Project one over the entire flux range probed. We also see no systematic offsets in this subset with distance from the phase center.

3.5. Astrometry

To assess our astrometric accuracy, we have compared the positions of 30 sources at 3 GHz with $S/N > 20$ with the positions detected in the Very Long Baseline Array (VLBA)-COSMOS 1.4 GHz survey (Herrera Ruiz et al. 2017). The matching radius used to find the 3 GHz sources in the Herrera Ruiz et al. (2017) catalog was $0''.4$. The results, shown in

Figure 9, yield an excellent agreement with a mean offset of $-0''.0001$ in $\Delta\text{R.A.}$ and $0''.02$ in $\Delta\text{decl.}$ We find a standard deviation of $0''.04$ for $\Delta\text{R.A.}$ and $0''.05$ for $\Delta\text{decl.}$ We note that we did not correct the catalog entries for the offsets found.

3.6. Completeness

To quantify the completeness of the catalog, we performed another set of Monte Carlo simulations where we added simulated sources to the pre-primary-beam-corrected image. Injecting sources into the image allows us to account for the varying noise across the field. We use the same approach as in Section 3.2, but when the position of the source is determined, the input flux density of the source is reduced, dependent on position within the primary beam. By doing this, we account for the decreasing sensitivity with increasing distance from the pointing center due to the primary beam attenuation. Because the beam sensitivity is not uniform and decreasing, the effective area over which we are sensitive to a given flux density S decreases rapidly with the flux density itself. By inserting primary beam-corrected flux densities, the derived completeness correction automatically includes the effect of variation of sensitivity as a function of distance from the map center.

To allow for a better estimate of the completeness in terms of integrated flux densities, the mock sources also include a percentage of extended sources: Gaussians with FWHM larger than the beam size. The mock sources get, therefore, also a major axis, minor axis and a S_{int} assigned. To generate an angular size distribution for the mock sources, we draw randomly from two skewed Gaussians, one for the major axis and one for the minor axis. These Gaussians are determined by fitting to the normalized distribution of the fitted Gaussian parameters as measured for the real sources by PyBDSF.

The total flux density was chosen to be either their integrated flux density, if resolved, or their peak brightness, if unresolved. To determine whether a simulated source was resolved or

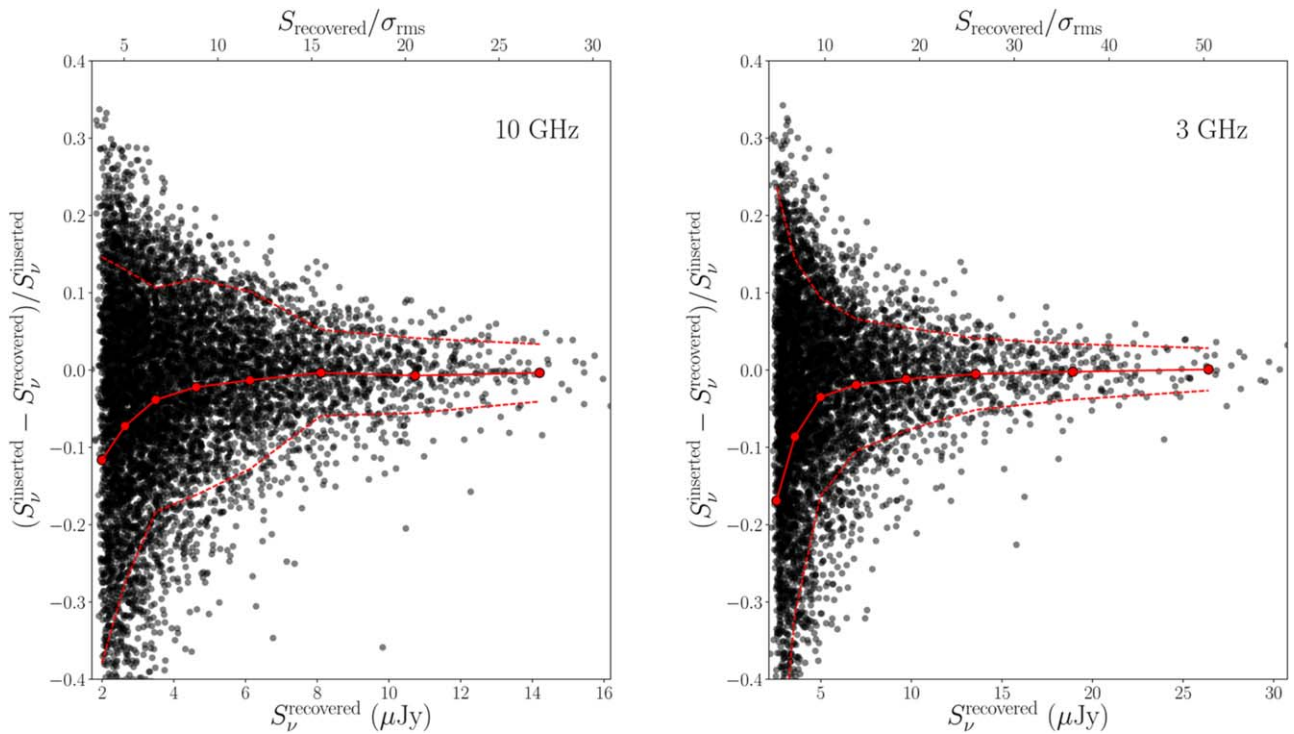


Figure 7. Simulated ratio of (inserted flux density – recovered flux density) to inserted flux density as a function of recovered flux density. The left panel shows the distribution for the 10 GHz image, and the right panel shows the distribution for the 3 GHz image. The solid red line denotes the median of eight logarithmic bins (indicated by the red points) across the flux density range, and the dashed lines mark the 1σ upper and lower bounds in those bins. The effect of flux boosting at the faint end is illustrated by the rapid downturn below about $3\ \mu\text{Jy}$ for 10 and 3 GHz.

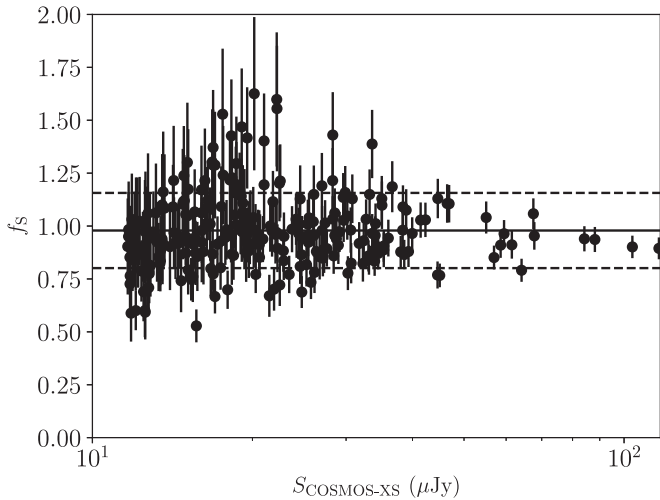


Figure 8. Flux comparison between our sample and the VLA-COSMOS 3 GHz Large Project (Smolčić et al. 2017b). The median ratio of 0.98 with a standard deviation of 0.18 shows that the flux densities are on the same flux scale.

unresolved, we use the same $S_{\text{int}}/S_{\text{peak}}$ envelope as described in Section 3.2.

Recovered mock sources are found by matching the retrieved catalog to the mock catalog. A retrieved source was considered to be matched with the inserted mock source if it was found within $0''.5$ of the inserted mock source position. Sources with a counterpart were flagged as recovered sources.

The completeness of a catalog represents the probability that all sources above a given flux density are detected. We have

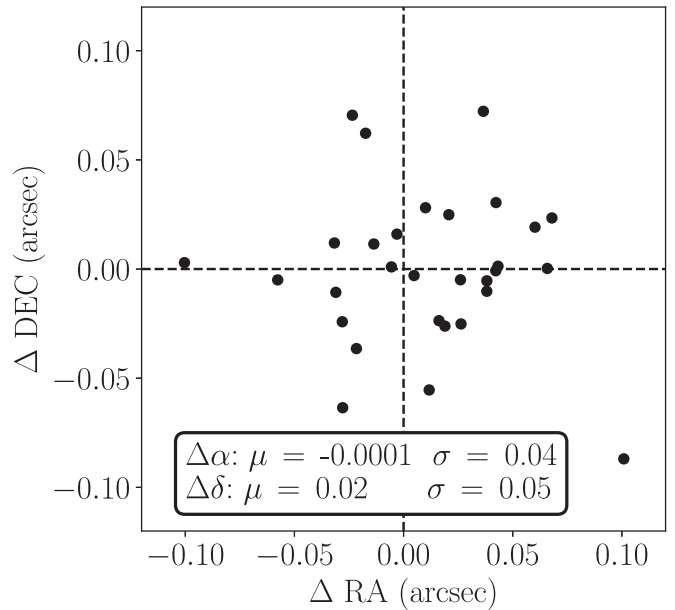


Figure 9. Astrometry comparison between 3 and 1.4 GHz VLBA data for 30 VLBA sources (Herrera Ruiz et al. 2017). Median and standard deviation for $\Delta\text{R.A.}$ and $\Delta\text{decl.}$ are reported in the panel. The positions of sources detected at 3 GHz are in excellent agreement with the positions as reported in the VLBA-COSMOS 1.4 GHz survey (Herrera Ruiz et al. 2017).

estimated this by giving the fraction of mock sources that are recovered using the same detection parameters. In Figure 11, we plot the fraction of detected sources in our simulation as a function of integrated flux density, accounting for the primary

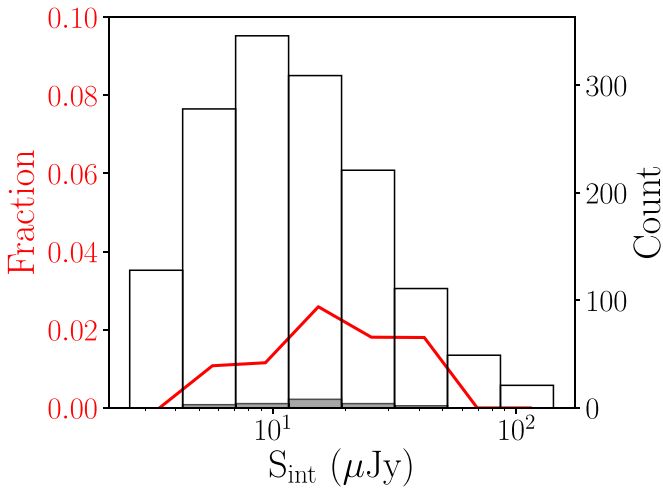


Figure 10. Fraction of false detections (red line) as a function of flux density. The open (filled) histogram shows the number of components cataloged in the observed 3 GHz map (detected in the inverted map). These data are also listed in Table 4. The false-detection rate is always smaller than 3% and is 1% overall.

beam. This detection fraction is largely driven by the variations in rms across the image and the primary beam. The error on the correction is the standard deviation of the calculated correction over all 200 realizations of the mock catalog. We thus estimate that the catalog is 85% complete above a flux density of $10 \mu\text{Jy}$ for the 10 GHz image and $15 \mu\text{Jy}$ for the 3 GHz image.

3.7. Reliability

The reliability of a source catalog indicates the probability that all sources above a given flux density are real sources and not accidental detections of background features or noise. To assess the false-detection rate of our source extraction, we ran PyBDSF on the inverted (i.e., multiplied by -1) continuum map within 20% of the peak primary beam sensitivity with the same settings used for the main catalog. Since there is no negative emission on the sky, every source detected in the inverted map is, by definition, a noise peak (i.e., a false detection). The false-detection rate is determined from the number ratio of negative sources over positive sources per flux density bin. Errors are calculated based on Poissonian errors on the number of sources per flux density bin.

For the inverted 10 GHz image, no sources were detected above our catalog threshold of 5σ ; thus, the false-detection rate was determined to be zero. The false-detection rate found for the 3 GHz image is shown in Figure 10 with the red line. The number counts for both the real and falsely detected sources are also shown. In total, there are 22 negative detections for the 3 GHz image, which results in a total false-detection rate of $\sim 1\%$. These sources are located around bright sources and are thus likely caused by the artifacts surrounding these sources.

3.8. Source Catalog

The final 10 GHz catalog consists of 91 sources, and the final 3 GHz catalog consists of 1481 sources. Both catalogs are available as a table in FITS format as part of the online version of this paper. Resolved sources are identified as described in Section 3.2. Errors given in the catalog are the nominal fit

errors reported by PyBDSF. A sample of the 3 GHz catalog is shown in Table 3.

4. Results

In this section, we report two results based on the produced catalogs: the 10 and 3 GHz faint source counts. Further analysis of these data will be presented in future publications.

4.1. Radio Source Counts

We use the 10 and 3 GHz catalogs to compute the source counts down to integrated flux densities of ~ 2 and $\sim 2.5 \mu\text{Jy}$, respectively.

The source counts are computed using the integrated flux densities (which means peak brightness for unresolved and integrated flux density for resolved), but sources are detected based on their measured peak brightness over the local noise level. The completeness of the source counts will thus depend both on the variation of the noise in the image and on the relation between integrated flux densities and peak brightness. In the following, we discuss these effects and how we correct for them in deriving the source counts.

4.1.1. Multicomponent Sources

Source counts need to take into account that sources may be made up of multiple components. For example, radio sources associated with radio galaxies can be made up of a nucleus with hot spots along or at the end of one or two jets. When jets are detected, it is relatively easy to recognize the components belonging to the same source. When a jet is missing, the radio lobes are detected as two separate sources. We apply the statistical technique described by Magliocchetti et al. (1998) and White et al. (2012) to find these double-component sources. We consider the separation of the nearest neighbor of each component and the summed flux density of the source and its neighbor. Multicomponents are combined as single sources if the ratio of their flux densities is between 0.25 and 4 and their separation is less than a critical value dependent on their integrated flux density, given by

$$\theta_{\text{crit}} = 100 \left(\frac{S_{\text{sum}}}{10} \right)^{0.5}, \quad (2)$$

where S_{sum} is in millijanskys and θ_{crit} is in arcseconds. This maximum separation is shown in Figure 12. We analyzed both the 10 and 3 GHz images but only found multicomponent sources for the 3 GHz image. The 3 GHz sources that meet both requirements are shown in Figure 12 as red circles. From this analysis, we could identify 17 multicomponent sources. See also Figure 17 for an example of a multicomponent source.

4.1.2. Completeness and Reliability

We consider a correction for the completeness of the catalog as derived in Section 3.6. Using the derived completeness corrections, we can calculate the source counts ($n(S)$) in each flux density bin using

$$n(S) = \frac{1}{A} \sum_{i=1}^N \frac{1}{C_{\text{compl}}(S_i)}, \quad (3)$$

where $A \sim 350 \text{ arcmin}^2$ is the solid angle considered for the source counts, N is the number of sources in the flux density

Table 3
Sample of the 3 GHz COSMOS-XS Catalog

Source ID	R.A.	$\sigma_{\text{R.A.}}$	Decl.	$\sigma_{\text{decl.}}$	S_{int}	S_{peak}	σ_{local}	Gaussians	Resolved
(1)	(deg)	(arcsec)	(deg)	(arcsec)	(μJy)	($\mu\text{Jy beam}^{-1}$)	($\mu\text{Jy beam}^{-1}$)	(11)	(12)
	(2)	(3)	(4)	(5)	(6-7)	(8-9)	(10)		
COSMOS-XS J100027.60+023634.21	150.11501	0.14907	2.6095	0.19592	4.04 ± 1.11	3.52 ± 0.67	0.65	S	U
COSMOS-XS J100014.35+023147.58	150.0598	0.03873	2.52988	0.04186	15.58 ± 1.03	13.74 ± 0.62	0.6	S	U
COSMOS-XS J100055.00+022849.80	150.22917	0.02603	2.4805	0.03019	52.54 ± 2.4	46.48 ± 1.44	1.41	S	R
COSMOS-XS J100031.26+023642.93	150.13026	0.03604	2.61192	0.04184	17.77 ± 1.16	16.04 ± 0.69	0.68	S	U
COSMOS-XS J100004.85+023559.51	150.02019	0.12507	2.59986	0.12439	7.01 ± 1.43	6.21 ± 0.85	0.84	S	U
COSMOS-XS J100056.66+022635.42	150.23607	0.02513	2.44317	0.03391	101.17 ± 3.56	76.85 ± 2.22	2.14	S	R
COSMOS-XS J100029.99+022903.64	150.12494	0.06062	2.48434	0.1729	5.85 ± 1.63	3.19 ± 0.66	0.66	M	U
COSMOS-XS J100046.61+023443.89	150.1942	0.2192	2.57886	0.10006	7.25 ± 1.37	5.54 ± 0.84	0.83	S	U
COSMOS-XS J100013.14+022550.66	150.05477	0.06633	2.43074	0.09338	22.27 ± 2.2	17.69 ± 1.34	1.32	S	R
COSMOS-XS J100004.59+023301.50	150.01914	0.05262	2.55042	0.06861	11.75 ± 1.31	11.05 ± 0.77	0.76	S	U

Note. The format is as follows. Column (1): source name. Columns (2) and (3): flux density–weighted R.A. and uncertainty. Columns (4) and (5): flux density–weighted decl. and uncertainty. Columns (6) and (7): integrated source flux density and uncertainty in μJy . Columns (8) and (9): peak brightness and uncertainty in $\mu\text{Jy beam}^{-1}$. Column (10): local rms noise. Column (11): number of Gaussian components; S refers to a single-Gaussian source, and M refers to a multi-Gaussian source. Column (12): flag indicating the resolved parameterization of the source; U refers to unresolved sources and R to resolved sources.

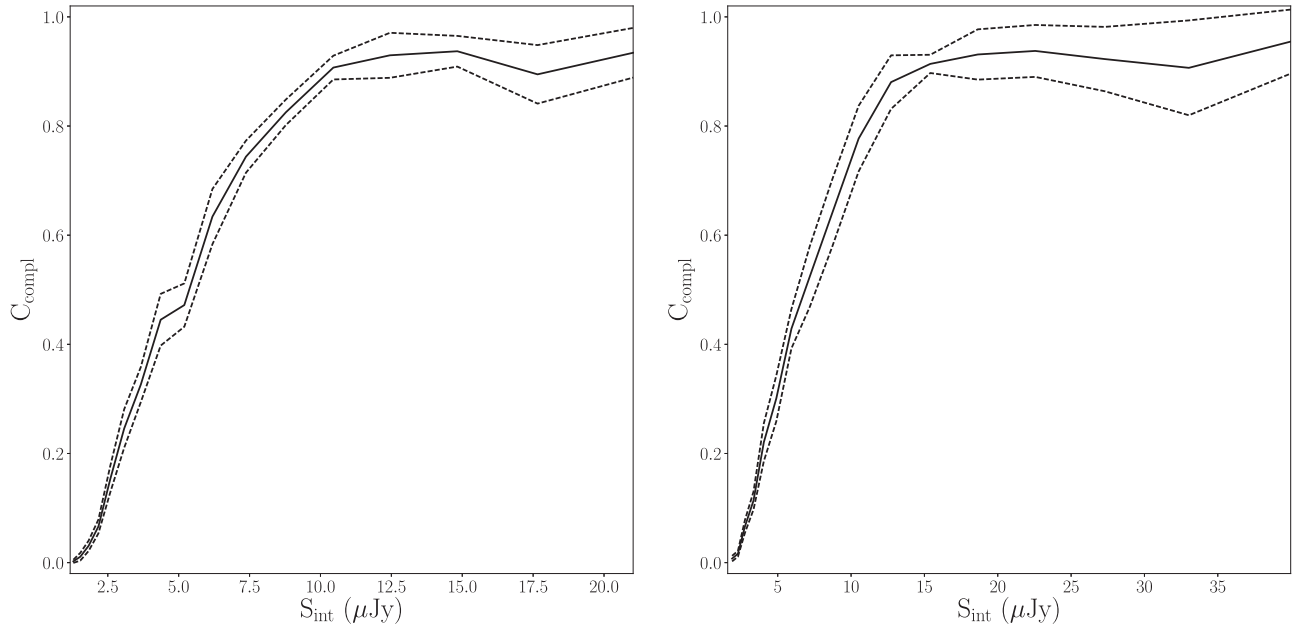


Figure 11. Completeness of the 10 (left) and 3 (right) GHz source catalog as a function of flux density. The solid black line shows the mean completeness of all Monte Carlo runs, and the dotted black lines show the standard deviation. The completeness is above $\sim 85\%$ for $10 \mu\text{Jy}$ for the 10 GHz source catalog. For the 3 GHz source catalog the completeness is above $\sim 85\%$ for $15 \mu\text{Jy}$. Note that the completeness does not reach 100% because the effects of the primary beam are also included.

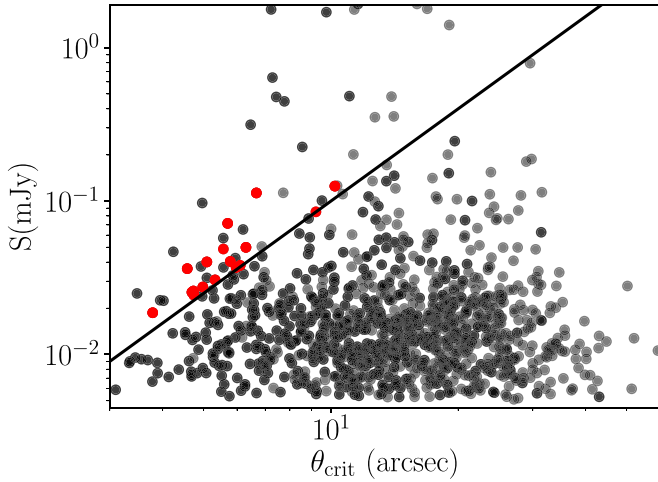


Figure 12. Sum of the flux densities of nearest-neighbor pairs as a function of their separation. Source pairs that have a separation less than the critical value given by the solid line and flux densities that differ by less than a factor of 4 are considered as double source candidates. Seventeen sources are identified as multicomponent sources and indicated with red points.

bin, and $C_{\text{compl}}(S_i)$ is the derived completeness for the given flux density.

Additionally, we make a correction for the reliability of the source counts at 3 GHz by applying the false-detection rate derived in Section 3.7. This correction acts in the opposite direction to the completeness correction and can be added to Equation (3),

$$n(S) = \frac{1}{A} \sum_{i=1}^N (1 - F_{\text{false-det}}(S_i)) \frac{1}{C_{\text{compl}}(S_i)}, \quad (4)$$

where A is the solid angle considered for the source counts, N is the number of sources in the flux density bin, $C_{\text{compl}}(S_i)$ is the

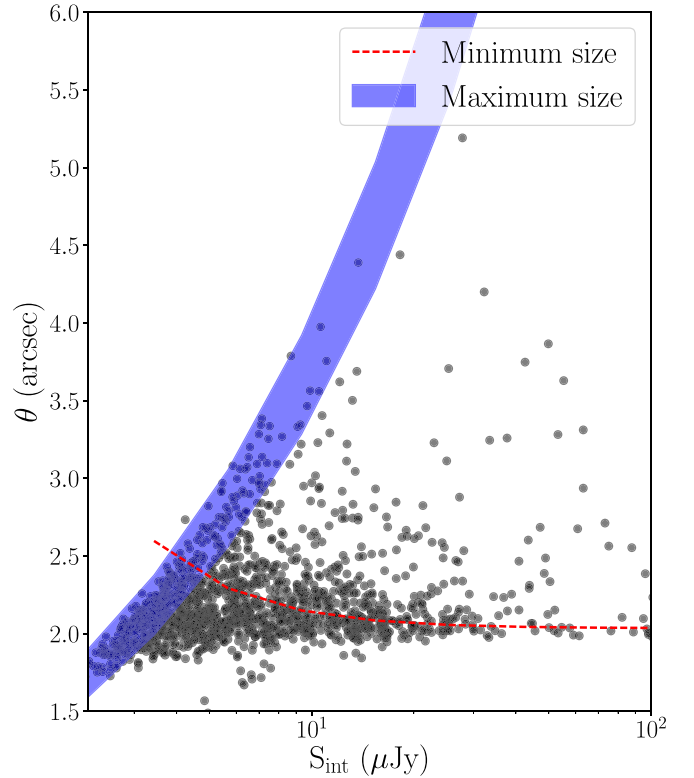


Figure 13. Fitted angular size, θ (geometric mean), as a function of integrated flux density at 3 GHz. Unresolved sources fall below the red dotted line giving the minimum size of a source. The minimum size was derived using the envelope from Section 3.2. The blue shaded region shows the maximum size a source of a given integrated flux density can have before dropping below the peak brightness detection threshold, where the range reflects the range of rms noise in the 3 GHz image.

derived completeness for the given flux density, and $F_{\text{false-det}}(S_i)$ is the correction for the false-detection rate for the given flux density bin.

4.1.3. Resolution Bias

Sources in our image are found by identifying peaks of emission above a given threshold. This means that a resolved source of a given integrated flux density will be missed more easily than a point source of the same integrated flux density. This incompleteness is called the resolution bias and causes the number of sources to be underestimated, particularly near the detection limit of the survey. We correct for the resolution bias by utilizing the analytic method as used in Prandoni et al. (2001) and Williams et al. (2016).

The following relation can be used to calculate the maximum angular size that a source can have and still be detected for a given integrated flux density:

$$S_{\text{int}}/5\sigma = \frac{\theta_{\text{min}}\theta_{\text{maj}}}{b_{\text{min}}b_{\text{maj}}}, \quad (5)$$

where θ_{min} and θ_{maj} are the fitted source axes as measured by PyBDSF, b_{min} and b_{maj} are the synthesized beam axes, and 5σ is the peak brightness detection limit (where σ is the local rms in the image). We use this relation to calculate the maximum size that a source can have and still be detected. This relation is shown in Figure 13, where the range reflects the range of rms noise in the image. Figure 13 also shows the distribution of θ , the geometric mean of the source major and minor axes, as a function of integrated flux density for all sources in the 3 GHz catalog. Also shown is the minimum size a source can have before it is deemed to be unresolved. We use the maximum size to calculate the fraction of sources expected to be larger than this value, following Windhorst et al. (1990), using

$$h(>\theta_{\text{max}}) = \exp\left[-\ln(2)\left(\frac{\theta_{\text{max}}}{\theta_{\text{med}}}\right)^{0.62}\right], \quad (6)$$

where θ_{max} is the maximum angular size and θ_{med} is the median angular size. The θ_{max} can be calculated by rewriting Equation (5):

$$\theta_{\text{max}} = \sqrt{b_{\text{min}}b_{\text{maj}} \times \frac{S_{\text{int}}}{5\sigma}}. \quad (7)$$

We use two different versions of θ_{med} for comparison; the first, given by Windhorst et al. (1990), is

$$\theta_{\text{med}} = 2(S_{1.4 \text{ GHz}})^{0.3''}, \quad (8)$$

with $S_{1.4 \text{ GHz}}$ in millijanskys (flux densities are scaled from 10 and 3 GHz to 1.4 GHz using a spectral index of -0.7), and the second used a constant size of $0''.35$ below 1 mJy (based on recent results from Cotton et al. 2018 and Bondi et al. 2018), as follows:

$$\theta_{\text{med}} = \begin{cases} 0''.35, & \text{for } S_{1.4 \text{ GHz}} < 1 \text{ mJy,} \\ 2(S_{1.4 \text{ GHz}})^{0.3''}, & \text{otherwise.} \end{cases} \quad (9)$$

We can calculate the resolution bias correction factor to be applied to the source counts using

$$c = 1/[1 - h(>\theta_{\text{max}})]. \quad (10)$$

The correction factors calculated using the two different size distributions are plotted as a function of 3 GHz S_{int} in Figure 14. We use the mean of the two correction factors to

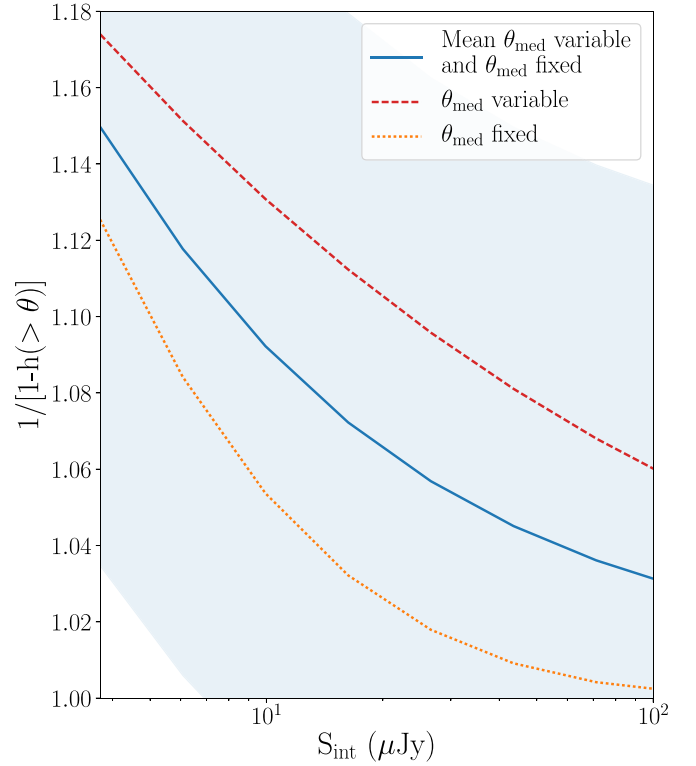


Figure 14. Resolution bias correction $1/[1 - h(>\theta_{\text{max}})]$ for the fraction of sources with angular size larger than θ_{max} at a given integrated flux density at 3 GHz. For the faintest sources, three curves are shown: the red dashed curve shows θ_{med} as a function of S_{int} , the orange dotted curve shows the result assuming $\theta_{\text{med}} = 0''.35$ at these flux densities, and the blue solid curve shows the mean of the two curves. The range reflects the assumed 10% uncertainty following Windhorst et al. (1990). The resolution bias correction is found to be 1.15 for the lowest flux bin.

correct the source counts in this paper, and this correction is calculated and applied for both the 10 and 3 GHz sources. We use the uncertainty in the forms of θ_{med} and θ_{max} to estimate the uncertainty in the resolution bias correction. We further include an overall 10% uncertainty following Windhorst et al. (1990) that dominates the error budget. We correct the resolution bias in the source count measurements by using the following to calculate the source counts in each flux density bin:

$$n(S) = \frac{1}{A} \sum_{i=1}^N (1 - F_{\text{false-det}}(S_i)) c(S_i) \frac{1}{C_{\text{compl}}(S_i)}, \quad (11)$$

where A is the solid angle considered for the source counts, N is the number of sources in the bin, $C_{\text{compl}}(S_i)$ is the derived completeness, and $c(S_i)$ is the resolution bias correction for the given flux density bin.

4.1.4. The Submicrojansky Source Counts at 3 GHz Compared to Observations

The Euclidean-normalized counts are shown in Figure 15(a) and tabulated in Table 4. Uncertainties on the final normalized source counts are propagated from the errors on the correction factors and the Poisson errors on the raw counts per bin. For the uncorrected data points, these errors are only the Poisson errors. Figure 15(a) illustrates our results compared to other observational

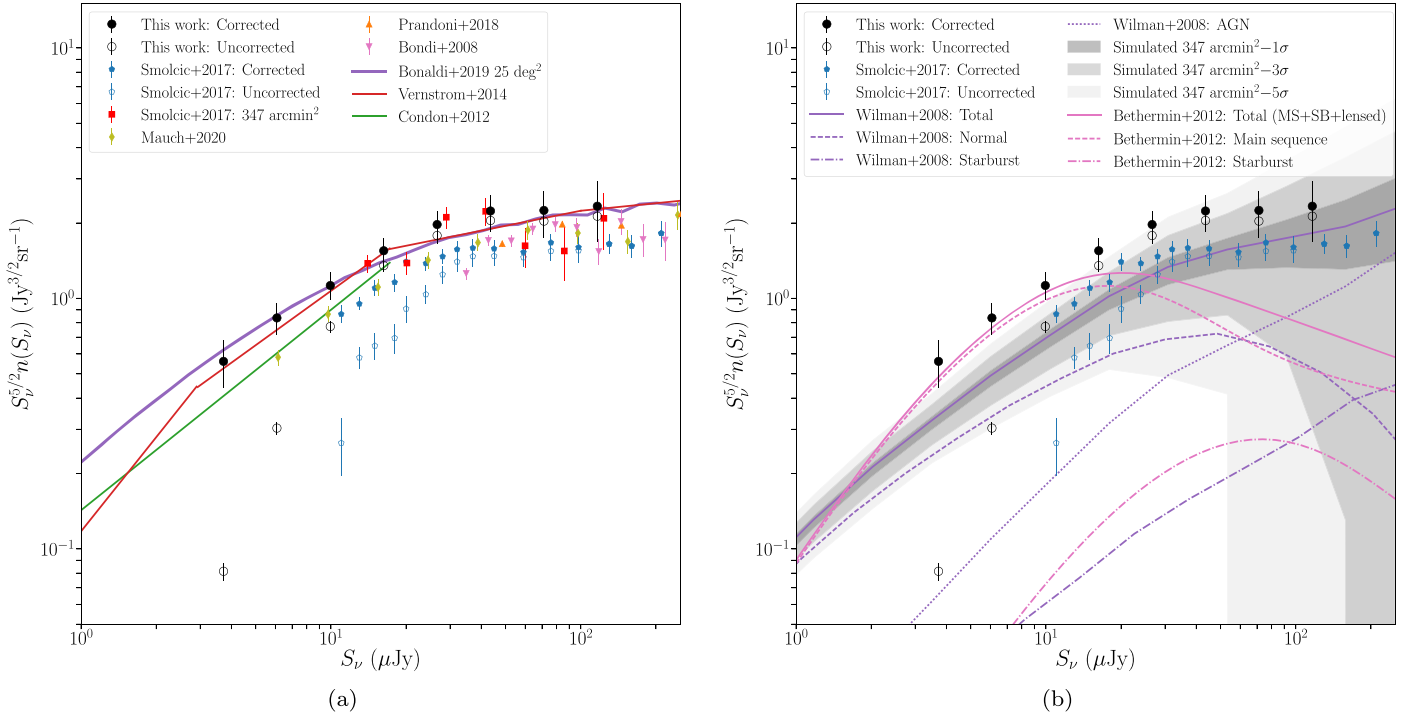


Figure 15. Euclidean-normalized radio source counts at 3 GHz (filled black circles). Open black circles show the source counts without corrections. Error bars correspond to the Poisson error for the uncorrected points. For the corrected points, the errors are propagated from the errors on the correction factors and the Poisson errors on the raw counts per bin. Corrected (filled) and uncorrected (open) VLA-COSMOS 3 GHz measurements from Smolčić et al. (2017b) are shown with blue points. Panel (a) also shows the number counts from $P(D)$ analysis by Condon et al. (2012; green line) and Vernstrom et al. (2014; red line). The purple line shows the results from the simulation of Bonaldi et al. (2019). The red filled squares show the source counts for sources in the Smolčić et al. (2017b) catalog within the area of our pointing. Panel (a) also shows the results from 1.4 GHz observations from Bondi et al. (2008; filled pink downward triangles) and Prandoni et al. (2018; filled orange upward triangles) and 1.28 GHz observations from Mauch et al. (2020; filled olive diamonds). The flux densities are shifted to the 3 GHz observed frame using a spectral index of -0.84 . Panel (b) shows the comparison to the number counts from the simulation of Wilman et al. (2008; purple lines) and Béthermin et al. (2012; pink lines). Different line styles correspond to different source types as defined in the legend. The solid lines show the total source counts. The shaded regions demonstrate the effect of cosmic variance and correspond to 1, 3, and 5 standard deviations in the source count measurements of the simulations by Wilman et al. (2008).

results, including the 3 GHz surveys by Condon et al. (2012), Vernstrom et al. (2014), and Smolčić et al. (2017b).

Condon et al. (2012) used the $P(D)$ (probability distribution of peak flux densities) analysis technique to statistically estimate the radio number counts down to $\sim 1 \mu\text{Jy}$ from VLA 3 GHz observations. The $P(D)$ analysis tends to be less prone to resolution effects, as it studies the statistical properties of sources well below the confusion limit of the survey. This approach results in statistical estimates of the source counts that are much fainter than the faintest sources that can be counted individually. Vernstrom et al. (2014) also used the $P(D)$ analysis technique to reanalyze the 3 GHz observations from Condon et al. (2012) and estimate the radio number counts down to $\sim 50 \text{ nJy}$. They used a different approach from Condon et al. (2012) that allowed for more flexibility in accurately modeling the true source counts. Our completeness-corrected points are slightly higher than the Condon et al. (2012) results and more consistent with the Vernstrom et al. (2014) results.

Smolčić et al. (2017b) derived source counts from 3 GHz observations of the 2 deg² COSMOS field in the VLA-COSMOS 3 GHz Large Project. For comparison, we show both the uncorrected number counts and number counts corrected for completeness, resolution bias, and false detections. Our

completeness-corrected points consistently lie a factor of ~ 1.4 above the source counts from Smolčić et al. (2017b).

One possible cause of the offset between our source counts and those of Smolčić et al. (2017b) is an underestimated correction for the resolution bias. In particular, our survey has a lower resolution than the Smolčić et al. (2017b) observation ($2''$ versus $0''.75$) and is therefore less likely to miss sources due to the resolution bias (see also the small correction derived in Section 4.1.3). Smolčić et al. (2017b) performed extensive Monte Carlo simulations to account for the resolution bias. They modeled the intrinsic angular sizes of mock sources using a simple power-law parameterization distribution of the angular sizes as a function of their total flux density, as derived by Bondi et al. (2008). They applied a minimum angular size for faint mock sources to ensure the modeled angular size distribution matched the observed size distribution. We tested whether the difference in resolution bias correction methods between Smolčić et al. (2017b) and that used here (described in Section 4.1.3) is significant, finding that when applied to the same data, our method results in a higher normalization than their method by a factor of ~ 1.1 (i.e., $\sim 25\%$ of the observed difference). Therefore, the difference in resolution bias correction method may partly explain the offset between our number counts and those reported in Smolčić et al. (2017b).

Table 4
Euclidean-normalized Differential Source Counts for the 3 GHz Catalog

ΔS_ν (μJy)	S_ν (μJy)	Counts ($\text{Jy}^{1.5}$ sr^{-1})	Error ($\text{Jy}^{1.5}$ sr^{-1})	N	$F_{\text{false-det}}$	C_{compt}	c
(1)	(2)	(3)	(4)	(5)	(6)	(7)	(8)
2.82–4.61	3.72	0.56	0.12	161	0.0	0.17	1.14
4.61–7.55	6.08	0.84	0.12	287	0.02	0.4	1.11
7.55–12.35	9.95	1.13	0.14	349	0.01	0.74	1.09
12.35–20.2	16.27	1.55	0.19	292	0.02	0.91	1.07
20.2–33.04	26.62	1.97	0.25	184	0.02	0.93	1.05
33.04–54.04	43.54	2.23	0.36	101	0.02	0.94	1.04
54.04–88.41	71.22	2.25	0.44	48	0.0	0.94	1.03
88.41–144.62	116.51	2.33	0.59	24	0.0	0.94	1.03

Note. The format is as follows. Column (1): flux interval. Column (2): bin center. Column (3): differential counts normalized to a non-evolving Euclidean mode. Column (4): error on differential counts. Column (5): number of sources detected. Column (6): false-detection rate. Column (7): completeness correction. Column (8): resolution bias correction. The listed differential counts were corrected for completeness and resolution bias (C_{compt} and c), as well as false-detection fractions ($F_{\text{false-det}}$), by multiplying the raw counts by the correction factor, which is equal to $(c(S_i) * (1 - F_{\text{false-det}}(S_i))) / C_{\text{compt}}(S_i)$. The source count errors take into account the Poissonian errors and completeness and bias correction uncertainties (see text for details).

To attempt to gain some additional insight, we also compare our results with those from recent 1.4 GHz (or similar) observations in Figure 15(a). We scale those flux densities to the 3 GHz observed frame assuming a spectral index of -0.84 .¹² Bondi et al. (2008) derived their counts in the inner 1 deg^2 region of the COSMOS field from the VLA-COSMOS 1.4 GHz Large Project (Schinnerer et al. 2007) catalog, which requires a somewhat uncertain correction for the effect of bandwidth smearing, while Prandoni et al. (2018) derived their counts from 1.4 GHz mosaic observations obtained with the Westerbork Synthesis Radio Telescope (WSRT). Because the latter cover an area of 6.6 deg^2 , the source catalog contains ~ 6000 sources (note that the error bars in Figure 15(a) are smaller than the symbols). Finally, Mauch et al. (2020) used the $P(D)$ analysis technique to derive source counts from 0.25 to $10 \mu\text{Jy}$ using confusion-limited 1.28 GHz MeerKAT observations. They further derived the source counts between $10 \mu\text{Jy}$ and 2.5 mJy from individual detected sources. The direct source counts (scaled to 3 GHz) are shown in Figure 15(a).

With the spectral index assumed (-0.84), we find that the source counts of Bondi et al. (2008), Prandoni et al. (2018), and Mauch et al. (2020) generally fall between those of Smolčić et al. (2017b) and those seen here and are, on average, lower than our source counts (particularly the Mauch et al. 2020 counts, which also extend to the lowest flux densities). As already noted by Smolčić et al. (2017b), the comparison between the 1.4 and 3 GHz source counts is complicated by the potentially overly simplistic scaling of the 3 GHz counts to 1.4 GHz using a single spectral index value (in addition to the varying resolution bias and bandwidth-smearing effects present). We therefore investigate one final effect that may influence the measured source counts in the following section.

4.1.5. Cosmic Variance

A final source of uncertainty that may affect the measured source counts is cosmic variance. In particular, if we observe overdensities in our single pointing, the resulting number

counts will be higher than the number counts averaged over a larger area (as done in Smolčić et al. 2017b).

Heywood et al. (2013) developed a method to assess the influence of source clustering on radio source counts. They extracted a series of independent samples from the models of Wilman et al. (2008). We used a similar approach with both the Wilman et al. (2008) and the Bonaldi et al. (2019) simulations, which are further discussed in the next section, to estimate the uncertainty induced by sample variance on a survey with the properties of our survey.

Following Heywood et al. (2013), we extract multiple nonoverlapping sky patches with areas of $0.31 \times 0.31 \text{ deg}^2$ from the Wilman et al. (2008) simulation (comparable to the effective area of our observations). We used a simulated area of $4 \times 4 \text{ deg}^2$. This process resulted in 169 source catalogs. For each of these simulated source subsets, we compute the Euclidean-normalized differential source counts. Figure 15(b) shows the mean value of the simulated counts from the independent distributions in each bin with a solid purple line. The shaded regions surrounding this correspond to one, three, and five times the standard deviation of the count measurements. Figure 15(b) shows that the count fluctuations found in our observed survey area are significant enough to dominate the observed scatter at flux densities above $100 \mu\text{Jy}$ and contribute significantly below this.

A similar approach was used to produce the shaded regions in Figure 16(a). Here we extract multiple nonoverlapping sky patches with areas of $0.31 \times 0.31 \text{ deg}^2$ from the simulation of Bonaldi et al. (2019). We used a simulated area of 25 deg^2 . This process results in 289 source catalogs. For each of these simulated source subsets, we compute the Euclidean-normalized differential source counts. The shaded regions in Figures 15(a) and 16(b) show that the offset between our number counts and the Smolčić et al. (2017b) counts could be at least partly explained by cosmic variance.

We are able to test this further using the fact that the Smolčić et al. (2017b) counts are derived from an area that also covers our pointing. By counting the sources in the Smolčić et al. (2017b) catalog within the area of our pointing and assuming the completeness corrections described in Smolčić et al. (2017b), we can compare their source density directly with our number counts. This comparison is shown in Figure 15(a).

¹² Smolčić et al. (2017b) found this spectral index by performing a Gaussian fit to the spectral index distribution of 3 GHz sources that were also detected at 1.4 GHz. This spectral index is different from the value derived using a survival analysis that takes nondetections into account. The difference can be explained by selection effects as discussed in Condon (1984).

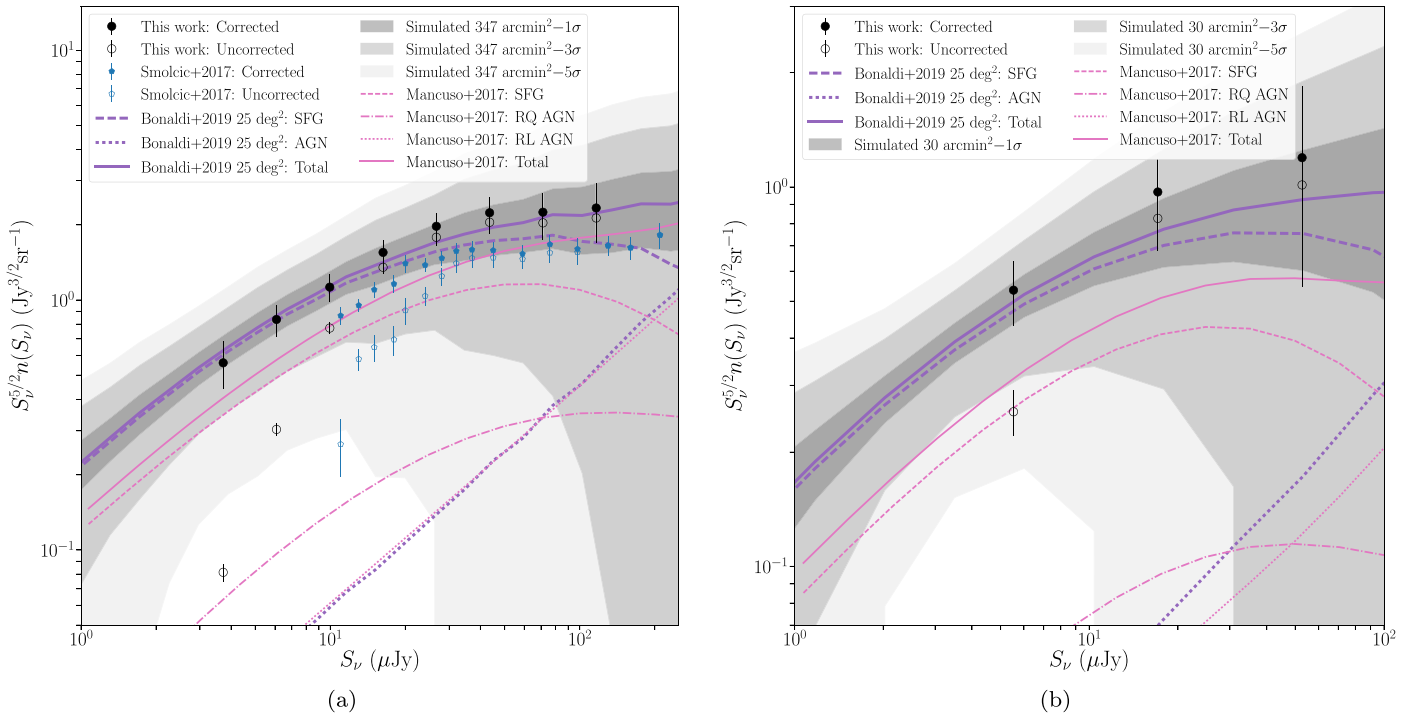


Figure 16. Euclidean-normalized radio source counts at 3 (panel (a)) and 10 (panel (b)) GHz. Filled black circles show the source counts from COSMOS-XS. Open black circles show the source counts without corrections. Error bars correspond to the Poisson error for the uncorrected points. For the corrected points, the errors are propagated from the errors on the correction factors and the Poisson errors on the raw counts per bin. Corrected (filled) and uncorrected (open) VLA-COSMOS 3 GHz measurements from Smolčić et al. (2017b) are shown with blue points. The number counts from the simulation of Bonaldi et al. (2019) and predictions from Mancuso et al. (2017) are shown with purple and pink lines, respectively. Different line styles correspond to different source types as defined in the legend. The solid lines show the total source counts from the simulation. The shaded regions demonstrate the effect of cosmic variance and correspond to 1, 3, and 5 standard deviations in the source count measurements of the simulations by Bonaldi et al. (2019).

The number counts in the Smolčić et al. (2017b) catalog over our pointing are noisy due to the small number statistics in this (shallower) sample, but they indicate a slightly higher source density (on average) within the area of our survey. We conclude that the systematic offset observed between our 3 GHz number counts and the 3 GHz direct detections from Smolčić et al. (2017b) can most likely be explained by a combination of cosmic variance in our pointing and an underestimated resolution bias correction in Smolčić et al. (2017b).

In summary, we find that our 3 GHz source counts agree with those at both 3 and 1.4 GHz within the various uncertainties while extending down to typically lower flux densities than previous direct detections. In the following section, we will therefore explore the implications of our derived source counts for the modeling of the ultrafaint radio population.

4.1.6. The Submicrojansky Source Counts at 3 GHz Compared to Simulations

In Figure 15(b), we compare our number counts with semianalytical models from Wilman et al. (2008) and Béthermin et al. (2012). Wilman et al. (2008) developed a semiempirical simulation that used observed and extrapolated luminosity functions (LFs) to populate an evolving dark matter skeleton with various galaxy types (normal, starburst, and AGN). The distribution of sources on the underlying dark matter density is done with biases, which reflects their measured large-scale clustering. The Béthermin et al. (2012) model uses two main

ingredients to predict the number counts: the evolution of MS and starburst galaxies based on the two-star formation-mode framework of Sargent et al. (2012) and MS and starburst SEDs to predict the shape of the IR LF at $z \leq 2$. Béthermin et al. (2012) also included dust attenuation and strong lensing in their model. To get to 1.4 GHz radio source counts, they assumed a nonevolving IR–radio correlation and a synchrotron spectral slope of $\alpha = -0.8$.

Our derived source counts deviate from those predicted by the Wilman et al. (2008) model. In particular, they tend to be higher than the predicted model from $\sim 40 \mu\text{Jy}$ downward (and we note that the Smolčić et al. 2017b counts are also systematically above this model at low flux densities, despite a possibly underestimated resolution bias correction; see Section 4.1.4). On the other hand, our 3 GHz source counts are in good agreement with the Béthermin et al. (2012) model below $\sim 10 \mu\text{Jy}$. The AGN population is not included in the Béthermin et al. (2012) model, and this explains the decrease in the source counts above $20 \mu\text{Jy}$, as AGNs start contributing significantly at these flux densities. Below $20 \mu\text{Jy}$, the star-forming population dominates the number counts, as can be seen from Figures 16(a) and 15(b). Béthermin et al. (2012) modeled this population using a framework that uses more recent results to predict the LF of SFGs at $z \leq 2$ compared to the Wilman et al. (2008) model. Béthermin et al. (2012) used a combination of mid-IR data, UV data (Daddi et al. 2007; Elbaz et al. 2007; Noeske et al. 2007), FIR data (Elbaz et al. 2011; Pannella et al. 2015), and radio continuum imaging (Karim et al. 2011). Wilman et al. (2008) assumed pure luminosity evolution out to $z = 1.5$ of the local LF derived from the IRAS

2 Jy sample by Yun et al. (2001). Our results suggest that the Wilman et al. (2008) model could be improved by using the most recent observations to derive a model for the LF for SFGs.

Bonaldi et al. (2019) developed an improved simulation in the spirit of that of Wilman et al. (2008): the Tiered Radio Extragalactic Continuum Simulation (T-RECS). Bonaldi et al. (2019) modeled the radio sky in terms of two main populations, AGNs and SFGs, and used these to populate an evolving dark matter skeleton. To describe the cosmological evolution of the LF of AGNs, they adopted an updated model of Massardi et al. (2010), with the revision of Bonato et al. (2017). The LF of SFGs is derived from the evolving SFR function as the radio continuum emission is correlated with the SFR. The SFR function gives the number density of galaxies per logarithmic bin of SFR at a given redshift z . The evolution of the synchrotron–SFR relation accounts for the evolving radio–FIR correlation. Bonaldi et al. (2019) used the SFR function with redshift derived by Cai et al. (2013, 2014) with an extension derived by Mancuso et al. (2015). The resulting SFR function now extends up to $z \sim 10$ and includes effects from strong gravitational lensing.

We compare the 3 GHz source counts to the simulation from Bonaldi et al. (2019) using the medium-tier catalog of 25 deg² containing 3 GHz flux densities. Our number counts, shown in Figure 16(a), match the total number counts from the simulations.

Figure 16(a) also shows the comparison between our source counts and those from the model by Mancuso et al. (2017). This model includes three populations: radio-loud (RL) AGNs, RQ AGNs, and SFGs. Using the same prescriptions as Bonaldi et al. (2019), they converted SFRs into 10 and 3 GHz luminosities. The SFR function used is, however, slightly different from the function used in Bonaldi et al. (2019; see Section 4.1.7). The RL AGNs are modeled the same way as in Bonaldi et al. (2019). To model RQ AGNs, the SFR function is mapped into the AGN luminosity function. The obtained AGN bolometric luminosity is subsequently converted to X-ray luminosity. The AGN radio power is then derived using the observed relation between rest-frame X-ray and 1.4 GHz radio luminosity for RQ AGNs.

The Mancuso et al. (2017) model uses an intrinsic SFR function and therefore claims to be less sensitive to dust extinction effects. The derived intrinsic SFR function implies a heavily dust-obscured galaxy population at high redshifts ($z > 4$) and large SFRs ($10^2 M_{\odot} \text{ yr}^{-1}$; Mancuso et al. 2016). Our number counts, shown in Figure 16(a), fall well above the total number counts predicted by Mancuso et al. (2017) at the faint end. In addition, there is a clear difference between the Bonaldi et al. (2019) simulations and the Mancuso et al. (2017) model, which is surprising, as they use similar assumptions. The difference between the two simulations is further discussed in Section 4.1.7.

To summarize, Wilman et al. (2008) modeled SFGs assuming pure luminosity evolution out to $z = 1.5$ for the local LF. Thereafter, there is no evolution for the LF. This model reproduces the sources in the local universe as it matches the observed number density. These sources dominate flux densities at >2 mJy. However, for flux densities <40 μ Jy, we find that the Béthermin et al. (2012) model and the Bonaldi et al. (2019) simulation are in better agreement with our observations. These models are able to produce the observed

Table 5
Euclidean-normalized Differential Source Counts for the 10 GHz Catalog

ΔS_{ν} (μ Jy)	S_{ν} (μ Jy)	Counts (Jy ^{1.5} sr ⁻¹)	Error (Jy ^{1.5} sr ⁻¹)	N	$F_{\text{false-det}}$	C_{compl}	c
(1)	(2)	(3)	(4)	(5)	(6)	(7)	(8)
2.71–8.36	5.53	0.53	0.1	52	0.0	0.53	1.1
8.36–25.8	17.08	0.97	0.22	31	0.0	0.9	1.06
25.8–79.66	52.73	1.2	0.65	7	0.0	0.88	1.04

Note. The format is as follows. Column (1): flux interval. Column (2): bin center. Column (3): differential counts normalized to a nonevolving Euclidean mode. Column (4): error on differential counts. Column (5): number of sources detected. Column (6): false-detection rate. Column (7): completeness correction. Column (8): resolution bias correction. The listed differential counts were corrected for completeness and resolution bias (C_{compl} and c), as well as false-detection fractions ($F_{\text{false-det}}$), by multiplying the raw counts by the correction factor, which is equal to $(c(S_i) * (1 - F_{\text{false-det}}(S_i))) / C_{\text{compl}}(S_i)$. The source count errors take into account the Poissonian errors and completeness and bias correction uncertainties (see text for details).

excess with respect to the source counts predicted by the Wilman et al. (2008) simulation. Our number counts support the steeper LF evolution for SFGs that is used in these models.

4.1.7. The Submicrojansky Source Counts at 10 GHz

The Euclidean-normalized counts at 10 GHz are shown in Figure 16(b). Uncertainties on the final normalized source counts are propagated from the errors on the correction factors and the Poisson errors on the raw counts per bin. The source counts are tabulated in Table 5.

With an observing frequency of 10 GHz, we measure flux densities closer to the rest-frame frequencies $\nu \geq 30$ GHz, where the total radio emission is dominated by free–free radiation (e.g., Condon 1992; Murphy et al. 2011; Klein et al. 2018). The calibration of the free–free radiation and SFR in the Bonaldi et al. (2019) simulations follows Mancuso et al. (2015) and Murphy et al. (2011). The Mancuso et al. (2017) model used the same calibration for SFGs.

We can compare the 10 GHz source counts to the simulation from Bonaldi et al. (2019) by interpolating between the flux densities of their simulated sources given at 9.2 and 12.5 GHz. Our number counts fall slightly above the total number counts from the simulations. The discrepancy is, however, within the σ derived for the cosmic variance, shown by the gray shaded regions in Figure 16(b). The shaded regions are derived in the same way as described in Section 4.1.5, by extracting sky patches of 0.09×0.09 deg² from the Bonaldi et al. (2019) simulations. This process results in 3025 source catalogs.

Our number counts are systematically higher than those predicted by Mancuso et al. (2017) at 10 GHz, especially at the faint end. This would indicate that Mancuso et al. (2017) underestimated the flux density produced at 10 GHz, especially by SFGs, as these contribute most at low flux densities, as can be seen in Figure 16(b).

As seen in Figures 16(a) and (b), the Bonaldi et al. (2019) and Mancuso et al. (2017) simulations predict roughly the same general shape of the number counts but a different normalization. The Mancuso et al. (2017) model includes the specific modeling of RQ AGNs. In the Bonaldi et al. (2019) simulations, RQ AGNs are not specifically modeled, and

Bonaldi et al. (2019) mentioned that RQ AGNs would contribute part of the flux density of those sources that, in T-RECS, are modeled as SFGs. Thus, this could not explain the difference in normalization between the total source counts.

Instead, the difference in normalization may be partially explained by how the two models treat the evolution of the radio–FIR correlation. Bonato et al. (2017) already showed that source counts support an evolving radio–FIR correlation. In their study, the source counts found without an evolving radio–FIR correlation are found to be substantially below the observational determinations. The Mancuso et al. (2017) model does not include the increase of the ratio between synchrotron and FIR luminosity, as was recently reported by Delhaize et al. (2017) and Magnelli et al. (2015), and thus falls below the observed source counts. Bonaldi et al. (2019) evolved the synchrotron–SFR relation to account for the evolving radio–FIR correlation, yielding a very good fit to the observational estimates of the radio luminosity function of SFGs (Novak et al. 2017).

In addition to their different treatment of the radio–FIR correlation, both the Mancuso et al. (2017) and Bonaldi et al. (2019) studies also use a slightly different SFR function to make number count predictions. In particular, both studies use a smooth, analytic representation of the SFR function derived from IR and dust extinction–corrected UV, Ly α , and H α data. However, Mancuso et al. (2017) used a standard Schechter shape characterized by three evolving parameters: the normalization, characteristic SFR, and faint-end slope. Meanwhile, Bonaldi et al. (2019) used the modified Schechter function introduced by Aversa et al. (2015), with two evolving characteristic slopes. Our observed number counts are in better agreement with the SFR function used by Bonaldi et al. (2019), which was derived by Mancuso et al. (2015), although the function used in Mancuso et al. (2017) was derived using the most recent IR and UV data.

In summary, as seen in Sections 4.1.6 and 4.1.7, models typically assume either an evolving LF or an evolving SFR function to make number count predictions at the microjansky level. We find that our source counts are in agreement with the Bonaldi et al. (2019) model that uses an evolving radio–FIR relation and the modified Schechter function to describe the SFR function. We also find that the source count predictions from the evolving LF for SFGs used by Béthermin et al. (2012) result in a good match with the observed number counts below 10 μ Jy.

The relation between the LF and the SFR functions will be investigated and presented in a future publication. The luminosity–SFR relation is of crucial importance for measuring the cosmic SFH, which will also be studied in a future publication. In addition, we can utilize the multiwavelength information available in the COSMOS region to determine the composition of the faint radio population responsible for the measured number counts. This will be fully discussed and presented in a companion paper (Algera et al. 2020).

5. Summary and Conclusions

In this paper, we presented the details of the COSMOS-XS survey: an ultradeep pointing in the COSMOS field at 10 and 3 GHz with the Karl G. Jansky VLA. The final 10 and 3 GHz images have a resolution of $\sim 2''$ and reach a median rms at the phase center of 0.41 and 0.53 μ Jy beam $^{-1}$, respectively.

The two radio catalogs contain sources detected within 20% of the peak primary beam sensitivity with peak brightness exceeding 5σ . The 10 GHz catalog contains 91 sources, and the 3 GHz catalog contains 1498 sources.

Comparing the positions of our 3 GHz sources with those from the high-resolution VLBA imaging at 1.4 GHz, we estimated that the astrometric uncertainties are negligible. Completeness corrections are calculated using Monte Carlo simulations, whereby the effect of the primary beam is taken into account. We find that the completeness is above $\sim 85\%$ at 10/15 μ Jy for the 10/3 GHz source catalogs, respectively. We correct for the resolution bias by utilizing an analytic method, as used in Prandoni et al. (2001) and Williams et al. (2016).

The deep 10 and 3 GHz observations enable us to investigate the Euclidean-normalized source counts down to the microjansky level. Our corrected radio counts at 3 GHz with direct detections down to $\sim 2.8 \mu$ Jy are consistent within the uncertainties with other results at 3 and 1.4 GHz but extend to fainter flux densities than previous direct detections.

In comparison to simulations developed in the framework of the SKA Simulated Skies project (Wilman et al. 2008), our source counts show an excess that cannot be accounted for by cosmic variance. Our measured source counts suggest a steeper LF evolution for SFGs for low flux densities (< 2 mJy). The T-RECS simulations (Bonaldi et al. 2019) and the Béthermin et al. (2012) model both produce this steeper evolution and are in better agreement with our measured source counts.

Our corrected radio counts at 10 GHz with direct detections down to $\sim 2.7 \mu$ Jy are systematically higher than those predicted by the T-RECS simulations (Bonaldi et al. 2019), but we demonstrate that this falls within the expected variations from cosmic variance. The more significant offset observed between our counts and Mancuso et al. (2017) supports an evolving radio–FIR relation and a modified Schechter function to describe the SFR function, as done in Bonaldi et al. (2019).

The COSMOS-XS survey is one of the deepest radio continuum surveys to date, providing valuable information for next-generation facilities, such as the ngVLA and SKA, which will achieve much deeper imaging. These radio data, in conjunction with the vast panchromatic COSMOS data sets, will allow us to study the dust-unbiased SFH, place critical constraints on dust attenuation, and conduct a study of the long-wavelength spectra of faint radio sources.

We thank the anonymous referee for helpful comments and suggestions that significantly improved this work. We thank Preshanth Jagannathan, Huib Intema, and Reinout van Weeren for the useful discussions that helped improve the imaging with WSclean; Chris Carilli for the useful discussions while preparing the proposal and for his help planning the observations; Mara Salvato for providing us with the COSMOS spectroscopic master catalog; Ian Smail for his comments; Andrea Lapi for providing the evolutionary track shown in Figures 16(a) and (b), which refers to the model discussed in Mancuso et al. (2017); and Paolo Ciliegi and Gianni Zamorani for useful discussion on previous 1.4 GHz source counts. The National Radio Astronomy Observatory is a facility of the National Science Foundation operated under cooperative agreement by Associated Universities, Inc. H.A., D.v.d.V., and J.H. acknowledge the support of the VIDI research program with project No. 639.042.611, which is (partly)

financed by the Netherlands Organisation for Scientific Research (NWO). D.R. acknowledges support from the National Science Foundation under grant No. AST-1614213. D.R. also acknowledges support from the Alexander von Humboldt Foundation through a Humboldt Research Fellowship for Experienced Researchers. This research made use of ASTROPY, a community-developed core Python package for astronomy (Astropy Collaboration et al. 2013, 2018) hosted at <http://www.astropy.org/>, matplotlib (Hunter 2007), numpy (van der Walt et al. 2011), scipy (Jones et al. 2001), and TOPCAT (Taylor 2005).

Software: ASTROPY (Astropy Collaboration et al. 2013, 2018), matplotlib (Hunter 2007), numpy (van der Walt et al. 2011), scipy (Jones et al. 2001), TOPCAT (Taylor 2005).

Appendix Postage-stamp Images

Examples of extended, multicomponent, and compact sources are shown in Figure 17.

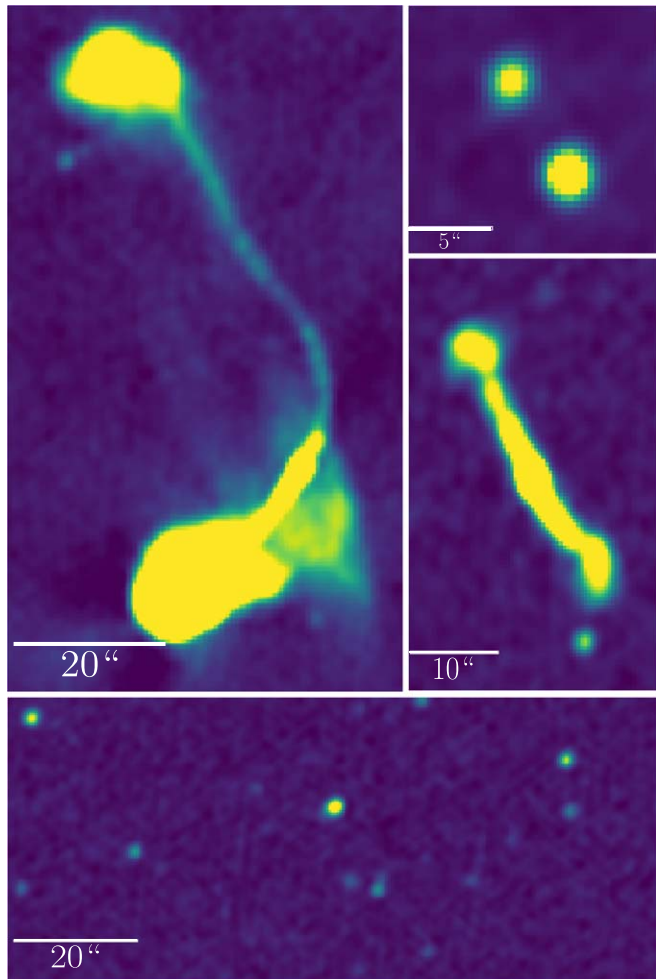


Figure 17. Stamps from the 3 GHz continuum map showing examples of extended (left and lower right), multicomponent (upper right), and compact (lower) radio sources. The color scale shows the flux density from $-3\sigma_{\text{local}}$ to $50\sigma_{\text{local}}$, where σ_{local} is the local rms noise.

ORCID iDs

H. S. B. Algera <https://orcid.org/0000-0002-4205-9567>
 J. A. Hodge <https://orcid.org/0000-0001-6586-8845>
 M. Novak <https://orcid.org/0000-0001-8695-825X>
 D. A. Riechers <https://orcid.org/0000-0001-9585-1462>
 F. Walter <https://orcid.org/0000-0003-4793-7880>

References

- Algera, H. S. B., van der Vlugt, D., Hodge, J. A., et al. 2020, *ApJ*, 903, 139
 Astropy Collaboration, Price-Whelan, A. M., Sipőcz, B. M., et al. 2018, *AJ*, 156, 123
 Astropy Collaboration, Robitaille, T. P., Tollerud, E. J., et al. 2013, *A&A*, 558, A33
 Aversa, R., Lapi, A., de Zotti, G., Shankar, F., & Danese, L. 2015, *ApJ*, 810, 74
 Bell, E. F. 2003, *ApJ*, 586, 794
 Best, P. N., Ker, L. M., Simpson, C., Rigby, E. E., & Sabater, J. 2014, *MNRAS*, 445, 955
 Béthermin, M., Daddi, E., Magdis, G., et al. 2012, *ApJL*, 757, L23
 Biggs, A. D., & Ivison, R. J. 2006, *MNRAS*, 371, 963
 Bonaldi, A., Bonato, M., Galluzzi, V., et al. 2019, *MNRAS*, 482, 2
 Bonato, M., Negrello, M., Mancuso, C., et al. 2017, *MNRAS*, 469, 1912
 Bondi, M., Ciliegi, P., Schinnerer, E., et al. 2008, *ApJ*, 681, 1129
 Bondi, M., Zamorani, G., Ciliegi, P., et al. 2018, *A&A*, 618, L8
 Bouwens, R. J., Bradley, L., Zitrin, A., et al. 2014, *ApJ*, 795, 126
 Bouwens, R. J., Illingworth, G. D., Oesch, P. A., et al. 2012, *ApJ*, 754, 83
 Bouwens, R. J., Illingworth, G. D., Oesch, P. A., et al. 2015, *ApJ*, 803, 34
 Briggs, D. S. 1995, AAS Meeting, 187, 112.02
 Brinchmann, J., Charlot, S., White, S. D. M., et al. 2004, *MNRAS*, 351, 1151
 Cai, Z.-Y., Lapi, A., Bressan, A., et al. 2014, *ApJ*, 785, 65
 Cai, Z.-Y., Lapi, A., Xia, J.-Q., et al. 2013, *ApJ*, 768, 21
 Calistro Rivera, G., Williams, W. L., Hardcastle, M. J., et al. 2017, *MNRAS*, 469, 3468
 Carilli, C. L., Lee, N., Capak, P., et al. 2008, *ApJ*, 689, 883
 Chary, R.-R., & Pope, A. 2010, arXiv:1003.1731
 Clemens, M. S., Vega, O., Bressan, A., et al. 2008, *A&A*, 477, 95
 Condon, J. J. 1984, *ApJ*, 287, 461
 Condon, J. J. 1992, *ARA&A*, 30, 575
 Condon, J. J., Cotton, W. D., & Broderick, J. J. 2002, *AJ*, 124, 675
 Condon, J. J., Cotton, W. D., Fomalont, E. B., et al. 2012, *ApJ*, 758, 23
 Condon, J. J., Cotton, W. D., Greisen, E. W., et al. 1998, *AJ*, 115, 1693
 Condon, J. J., & Mitchell, K. J. 1984, *AJ*, 89, 610
 Cotton, W. D., Condon, J. J., Kellermann, K. I., et al. 2018, *ApJ*, 856, 67
 Daddi, E., Dickinson, M., Morrison, G., et al. 2007, *ApJ*, 670, 156
 de Jong, T., Klein, U., Wielebinski, R., & Wunderlich, E. 1985, *A&A*, 147, L6
 Delhaize, J., Smolčić, V., Delvecchio, I., et al. 2017, *A&A*, 602, A4
 Delvecchio, I., Gruppioni, C., Pozzi, F., et al. 2014, *MNRAS*, 439, 2736
 Delvecchio, I., Smolčić, V., Zamorani, G., et al. 2017, *A&A*, 602, A3
 Dumas, G., Schinnerer, E., Tabatabaei, F. S., et al. 2011, *AJ*, 141, 41
 Elbaz, D., Daddi, E., Le Borgne, D., et al. 2007, *A&A*, 468, 33
 Elbaz, D., Dickinson, M., Hwang, H. S., et al. 2011, *A&A*, 533, A119
 Helou, G., Soifer, B. T., & Rowan-Robinson, M. 1985, *ApJL*, 298, L7
 Herrera Ruiz, N., Middelberg, E., Deller, A., et al. 2017, *A&A*, 607, A132
 Heywood, I., Jarvis, M. J., & Condon, J. J. 2013, *MNRAS*, 432, 2625
 Hickox, R. C., Jones, C., Forman, W. R., et al. 2009, *ApJ*, 696, 891
 Hunter, J. D. 2007, *CSE*, 9, 90
 Huynh, M. T., Jackson, C. A., Norris, R. P., & Prandoni, I. 2005, *AJ*, 130, 1373
 Ilbert, O., McCracken, H. J., Le Fèvre, O., et al. 2013, *A&A*, 556, A55
 Jarvis, M., Seymour, N., Afonso, J., et al. 2015, in Proc. of Advancing Astrophysics with the Square Kilometre Array (AASKA14) (Trieste: PoS), 68
 Jarvis, M. J., & Rawlings, S. 2000, *MNRAS*, 319, 121
 Jones, E., Oliphant, T., Peterson, P., et al. 2001, SciPy: Open Source Scientific Tools for Python, <http://www.scipy.org/>
 Karim, A., Schinnerer, E., Martínez-Sansigre, A., et al. 2011, *ApJ*, 730, 61
 Klein, U., & Graeve, R. 1986, *A&A*, 161, 155
 Klein, U., Lisenfeld, U., & Verley, S. 2018, *A&A*, 611, A55
 Kobulnicky, H. A., & Johnson, K. E. 1999, *ApJ*, 527, 154
 Kurczynski, P., Gawiser, E., Acquaviva, V., et al. 2016, *ApJL*, 820, L1
 Madau, P., & Dickinson, M. 2014, *ARA&A*, 52, 415

- Magdis, G. E., Elbaz, D., Hwang, H. S., et al. 2010, *ApJL*, **720**, L185
- Magliocchetti, M., Maddox, S. J., Lahav, O., & Wall, J. V. 1998, *MNRAS*, **300**, 257
- Magnelli, B., Ivison, R. J., Lutz, D., et al. 2015, *A&A*, **573**, A45
- Mancuso, C., Lapi, A., Cai, Z.-Y., et al. 2015, *ApJ*, **810**, 72
- Mancuso, C., Lapi, A., Prandoni, I., et al. 2017, *ApJ*, **842**, 95
- Mancuso, C., Lapi, A., Shi, J., et al. 2016, *ApJ*, **823**, 128
- Massardi, M., Bonaldi, A., Negrello, M., et al. 2010, *MNRAS*, **404**, 532
- Mauch, T., Cotton, W. D., Condon, J. J., et al. 2020, *ApJ*, **888**, 61
- McAlpine, K., Jarvis, M. J., & Bonfield, D. G. 2013, *MNRAS*, **436**, 1084
- Mendez, A. J., Coil, A. L., Aird, J., et al. 2013, *ApJ*, **770**, 40
- Mezger, P. G., & Henderson, A. P. 1967, *ApJ*, **147**, 471
- Mohan, N., & Rafferty, D. 2015, PyBDSF: Python Blob Detection and Source Finder, Astrophysics Source Code Library, v1.9.1, ascl:1502.007
- Morrison, G. E., Owen, F. N., Dickinson, M., Ivison, R. J., & Ibar, E. 2010, *ApJS*, **188**, 178
- Murphy, E. J., Bremseth, J., Mason, B. S., et al. 2012, *ApJ*, **761**, 97
- Murphy, E. J., Condon, J. J., Schinnerer, E., et al. 2011, *ApJ*, **737**, 67
- Murphy, E. J., Dong, D., Leroy, A. K., et al. 2015, *ApJ*, **813**, 118
- Murphy, E. J., Momjian, E., Condon, J. J., et al. 2017, *ApJ*, **839**, 35
- Nayyeri, H., Hemmati, S., Mobasher, B., et al. 2017, *ApJS*, **228**, 7
- Nikolic, B., & Bolton, R. C. 2012, *MNRAS*, **425**, 1257
- Noeske, K. G., Weiner, B. J., Faber, S. M., et al. 2007, *ApJL*, **660**, L43
- Novak, M., Smolčić, V., Delhaize, J., et al. 2017, *A&A*, **602**, A5
- Offringa, A. R. 2010, AOfFlagger: RFI Software, Astrophysics Source Code Library, v2.9.0, ascl:1010.017
- Offringa, A. R., McKinley, B., Hurley-Walker, N., et al. 2014, WSClean: Widefield interferometric imager, Astrophysics Source Code Library, v2.5, ascl:1408.023
- Offringa, A. R., & Smirnov, O. 2017, *MNRAS*, **471**, 301
- Owen, F. N. 2018, *ApJS*, **235**, 34
- Owen, F. N., & Morrison, G. E. 2008, *AJ*, **136**, 1889
- Padovani, P., Bonzini, M., Kellermann, K. I., et al. 2015, *MNRAS*, **452**, 1263
- Padovani, P., Mainieri, V., Tozzi, P., et al. 2009, *ApJ*, **694**, 235
- Pannella, M., Carilli, C. L., Daddi, E., et al. 2009, *ApJL*, **698**, L116
- Pannella, M., Elbaz, D., Daddi, E., et al. 2015, *ApJ*, **807**, 141
- Pavesi, R., Sharon, C. E., Riechers, D. A., et al. 2018, *ApJ*, **864**, 49
- Perley, R. A., & Butler, B. J. 2013, *ApJS*, **204**, 19
- Prandoni, I., Gregorini, L., Parma, P., et al. 2001, *A&A*, **365**, 392
- Prandoni, I., Guglielmino, G., Morganti, R., et al. 2018, *MNRAS*, **481**, 4548
- Rau, U., & Cornwell, T. J. 2011, *A&A*, **532**, A71
- Richards, E. A. 2000, *ApJ*, **533**, 611
- Riechers, D. A., Pavesi, R., Sharon, C. E., et al. 2019, *ApJ*, **872**, 7
- Rigby, E. E., Best, P. N., Brookes, M. H., et al. 2011, *MNRAS*, **416**, 1900
- Rowan-Robinson, M., Benn, C. R., Lawrence, A., McMahon, R. G., & Broadhurst, T. J. 1993, *MNRAS*, **263**, 123
- Rujopakarn, W., Dunlop, J. S., Rieke, G. H., et al. 2016, *ApJ*, **833**, 12
- Sabater, J., Best, P. N., Hardcastle, M. J., et al. 2019, *A&A*, **622**, A17
- Sadler, E. M., Jenkins, C. R., & Kotanyi, C. G. 1989, *MNRAS*, **240**, 591
- Salim, S., Rich, R. M., Charlot, S., et al. 2007, *ApJS*, **173**, 267
- Salmon, B., Papovich, C., Finkelstein, S. L., et al. 2015, *ApJ*, **799**, 183
- Sargent, M. T., Béthermin, M., Daddi, E., & Elbaz, D. 2012, *ApJL*, **747**, L31
- Schinnerer, E., Sargent, M. T., Bondi, M., et al. 2010, *ApJS*, **188**, 384
- Schinnerer, E., Smolčić, V., Carilli, C. L., et al. 2007, *ApJS*, **172**, 46
- Schreiber, C., Pannella, M., Elbaz, D., et al. 2015, *A&A*, **575**, A74
- Seymour, N., Dwelly, T., Moss, D., et al. 2008, *MNRAS*, **386**, 1695
- Seymour, N., McHardy, I. M., & Gunn, K. F. 2004, *MNRAS*, **352**, 131
- Siana, B., Smail, I., Swinbank, A. M., et al. 2009, *ApJ*, **698**, 1273
- Siana, B., Teplitz, H. I., Chary, R.-R., Colbert, J., & Frayer, D. T. 2008, *ApJ*, **689**, 59
- Smolčić, V., Delvecchio, I., Zamorani, G., et al. 2017a, *A&A*, **602**, A2
- Smolčić, V., Novak, M., Bondi, M., et al. 2017b, *A&A*, **602**, A1
- Smolčić, V., Schinnerer, E., Zamorani, G., et al. 2009a, *ApJ*, **690**, 610
- Smolčić, V., Zamorani, G., Schinnerer, E., et al. 2009b, *ApJ*, **696**, 24
- Speagle, J. S., Steinhardt, C. L., Capak, P. L., & Silverman, J. D. 2014, *ApJS*, **214**, 15
- Tabatabaei, F. S., Schinnerer, E., Krause, M., et al. 2017, *ApJ*, **836**, 185
- Taylor, M. B. 2005, in ASP Conf. Ser. 347, Astronomical Data Analysis Software and Systems XIV, ed. P. Shopbell, M. Britton, & R. Ebert (San Francisco, CA: ASP), 29
- Tomczak, A. R., Quadri, R. F., Tran, K.-V. H., et al. 2016, *ApJ*, **817**, 118
- Turner, J. L., & Ho, P. T. P. 1983, *ApJL*, **268**, L79
- Turner, J. L., & Ho, P. T. P. 1985, *ApJL*, **299**, L77
- van der Walt, S., Colbert, S. C., & Varoquaux, G. 2011, *CSE*, **13**, 22
- Vernstrom, T., Scott, D., Wall, J. V., et al. 2014, *MNRAS*, **440**, 2791
- Vernstrom, T., Scott, D., Wall, J. V., et al. 2016, *MNRAS*, **462**, 2934
- White, G. J., Hatsukade, B., Pearson, C., et al. 2012, *MNRAS*, **427**, 1830
- Williams, W. L., van Weeren, R. J., Röttgering, H. J. A., et al. 2016, *MNRAS*, **460**, 2385
- Wilman, R. J., Miller, L., Jarvis, M. J., et al. 2008, *MNRAS*, **388**, 1335
- Windhorst, R., Mathis, D., & Neuschaefer, L. 1990, in ASP Conf. Ser. 10, Evolution of the Universe of Galaxies, ed. R. G. Kron (San Francisco, CA: ASP), 389
- Yun, M. S., Reddy, N. A., & Condon, J. J. 2001, *ApJ*, **554**, 803